

Polarization Diagnostics Applied to Coronal Mass Ejections and the Background Solar Wind

Sarah E. Gibson¹ · · Craig E. DeForest² · ·
Curt A. de Koning³ ·
Steven R. Cranmer⁴ · · Yuhong Fan¹ ·
Huw Morgan⁵ · Elena Provornikova⁶ ·
Anna Malanushenko¹ · David Webb⁷

© The author(s) · · · ·

S.E. Gibson
sgibson@ucar.edu
C.E. DeForest
deforest@boulder.swri.edu
C.A. de Koning
dekoning@colorado.edu
S.R. Cranmer
steven.cranmer@colorado.edu
Y. Fan
fan@ucar.edu
H. Morgan
hum2@aber.ac.uk
E. Provornikova
elena.provornikova@jhupl.edu
A. Malanushenko
anny@ucar.edu
D. Webb
david.webb@bc.edu

- ¹ High Altitude Observatory, National Center for Atmospheric Science, Boulder, CO, 80301, USA
- ² Southwest Research Institute, Boulder, CO, 80301, USA
- ³ CIRES, University of Colorado, Boulder, CO, 80301, USA
- ⁴ Department of Astrophysical and Planetary Sciences, Laboratory for Atmospheric and Space Physics, University of Colorado, Boulder, CO, USA
- ⁵ Aberystwyth University, Aberystwyth, UK
- ⁶ Applied Physics Laboratory, Johns Hopkins University, Laurel, MD, USA

arXiv:2511.00714v1 [astro-ph.SR] 1 Nov 2025

Abstract

The ratio of radially to tangentially polarized Thomson-scattered white light provides a powerful tool for locating the 3D position of compact structures in the solar corona and inner heliosphere, and the Polarimeter to Unify the Corona and Heliosphere (PUNCH) has been designed to take full advantage of this diagnostic capability. Interestingly, this same observable that establishes the position of transient blob-like structures becomes a local measure of the slope of the global falloff of density in the background solar wind. It is thus important to characterize the extent along the line of sight of structures being studied, in order to determine whether they are sufficiently compact for 3D positioning. In this paper, we build from analyses of individual lines of sight to three-dimensional models of coronal mass ejections (CMEs), allowing us to consider how accurately polarization properties of the transient and quiescent solar wind are diagnosed. In this way, we demonstrate the challenges and opportunities presented by PUNCH polarization data for various quantitative diagnostics.

1. Introduction

The Polarimeter to Unify the Corona and Heliosphere, or PUNCH, is a NASA Small Explorer Mission. PUNCH studies the “young” solar wind, by obtaining direct, continuous 3D imaging of the entire corona and inner heliosphere in polarized white light via four synchronous smallsats. It launched in March, 2025, with a two-year prime mission duration. See DeForest et al. (2025) for an overview of the mission, its instruments, and its scientific objectives.

A primary science target for PUNCH is characterizing Coronal Mass Ejections (CMEs; see, e.g., Malanushenko et al. (2025)) which are generally expected to incorporate coherently twisted magnetic fields, i.e., magnetic flux ropes (see, e.g., Provornikova et al. (2025)). PUNCH provides a full-circle field of view (FOV) from five solar radii outward, mosaicking the fields of view of a central Near Field Imager (NFI) (Colaninno et al., 2025) with three Wide Field Imagers (WFI) (Laurent, 2025). In this way, PUNCH fills existing gaps between coronagraphs and heliospheric imagers and obtains continuous wide-field observations of the evolution of CMEs and their substructure from the Sun throughout the inner solar system. This large FOV is also intended to yield new insight into the formation, evolution and 3D structure of stream interaction regions (SIRs) that arise between fast and slow wind streams (de Koning et al., 2025).

PUNCH obtains both brightness and polarized brightness measurements to image and locate evolving SIR and CME structures in 3D: a measurement of great importance to space weather predictions (Seaton et al., 2025). Until PUNCH, only coronagraphs (i.e., no heliospheric imagers) have had both brightness and polarized brightness observations. PUNCH is the first heliospheric imager to be designed with polarization capability and to have the sensitivity, spatial FOV, and polarization capability needed to locate and track bright

⁷ Institute for Scientific Research, Boston College, Chestnut Hill, MA, USA

structures as they propagate, with both its inner coronagraph and its three heliospheric imagers operating as a single “virtual instrument”.

In Section 2 we review how these data may be directly related to a 3D position of a compact mass, or “superparticle”, along a particular line of sight. We also consider how the same image data can provide a completely different diagnostic, a local measure of the global falloff of the background solar wind density. We discuss the transition between these two extremes and how the viewing angle on a compact mass and its width along a line of sight affects the ability to establish its 3D location via polarization, and discuss unavoidable uncertainties in polarization analysis due to the size and location of a scattering mass.

In Section 3, we present a variety of forward modeled CMEs, comparing the 3D position of the CME front to ground truth simulation knowledge of the position of mass along the line of sight. We also discuss how front-back ambiguity associated with polarization analysis can be resolved using the wide field of view and sensitivity of PUNCH images, and how establishing the 3D position of CME substructures might be used to diagnose magnetic flux rope chirality.

In Section 4, we present our conclusions.

2. Polarization Diagnostics

2.1. Background

The brightness and polarization of the white light corona was first considered theoretically by Schuster (1879), and then in comparison to observations of solar eclipses (Young, 1911; Minnaert, 1930; Baumbach, 1938; Öhman, 1947; van de Hulst, 1950). These analyses demonstrated how radiation from the solar photosphere is Thomson scattered in the optically-thin corona, and how the linearly polarized component of that radiation (polarized brightness, or pB) becomes an excellent diagnostic of the line-of-sight integral of n_e (see also Altschuler and Perry, 1972; Munro and Jackson, 1977; Inhester, 2015). The fall-off with distance of $n_e(r)$ has been studied using pB by multiple authors, including Saito et al. (1970); Munro and Jackson (1977); Fisher and Guhathakurta (1995); Guhathakurta, Holzer, and MacQueen (1996); Gibson et al. (1999); Edwards et al. (2023). Others have combined coronagraph data with radio and in-situ measurements to find density parameterizations that cover distances from the low corona to interplanetary space (e.g., Bird and Edenhofer, 1990; Leblanc, Dulk, and Bougeret, 1998; Mann et al., 2023).

Many of the density diagnostic studies cited above used observations of pB from ground-based coronagraphs. Total brightness (tB) – i.e., the sum of radial and tangential brightnesses – is difficult to measure from the ground because of the largely unpolarized sky brightness background (except during a solar eclipse). With the launch of space-based coronagraphs, it became possible to routinely observe both pB and tB , making it possible to establish the position along the line of sight of a “superparticle”, as described in the next section.

We note that at least two definitions of pB have entered the literature, as more fully detailed in DeForest, Seaton, and West (2022). In this paper, we consider pB

polarized in the inner corona (elongation angles $\varepsilon < 5 - 10^\circ$), and so it does not contribute significantly to pB there (Lamy et al., 2020). However, the F-corona does become polarized to approximately 7% at larger distances (Morgan and Cook, 2020). Further, total brightness (tB) includes unpolarized light and so has a contribution from the F-corona at all heights. Fortunately, the F-corona is very smooth compared to the K-corona, and robust methods have been established to model and remove it from both pB and tB (Morgan and Cook, 2020; Lamy et al., 2021; Lamy, Gilardy, and Llebaria, 2022).

2.2. Locating Position of Superparticles

Studies of the corona close to the Sun are able to use the approximation that the set of line-of-sight observing rays are all parallel to one another. In that limit, one can also define the “plane of the sky” (POS) as the plane perpendicular to those rays that also contains the center of the Sun. However, for large elongation angles (as observed by PUNCH’s Wide Field Imagers) this limit no longer applies and it makes more sense to refer to the Thomson Surface (TS; Figure 1), sometimes called the Thomson Sphere, as the locus of points that generally maximize the optically thin scattering signal (see, e.g., Vourlidas and Howard, 2006; Howard and DeForest, 2012; Howard et al., 2013; DeForest, Howard, and Tappin, 2013a).

Bearing this in mind, we now consider a compact mass, or superparticle, in 3D Cartesian coordinates, as shown in Figure 1. (We will explicitly define conditions where a structure’s central position can be found, such that it may be considered “localized”, in Section 2.5.) The line-of-sight elongation angle ε gives the radial distance r_{pos} projected on the $Y - Z$ plane, and this along with the object’s projected position angle α allows us to calculate a projected (or, for small ε , actual) Y and Z position, as shown in the bottom left insert of Figure 1. To find the 3D position we then need to determine the object’s position x along the X axis. As we show below, the *degree of polarization*, $p \equiv pB/tB$, can be directly related to the scattering angle χ of light off of the object. χ is the complement of τ , the angular position of the object along the line of sight from the TS, and x can be determined from either χ or τ , in combination with ε (see Section 2.2.2). The full 3D Cartesian position, x, y, z is thus established.

This property of polarization has been exploited in previous works, (e.g., Hildner et al., 1975; Poland and Munro, 1976; Crifo, Picat, and Cailloux, 1983; Moran and Davila, 2004; Dere, Wang, and Howard, 2005; Moran, Davila, and Thompson, 2010; Mierla et al., 2009, 2010; Mierla et al., 2011; Dai et al., 2014; Chifu, 2015; Pagano, Bemporad, and Mackay, 2015; Bemporad and Pagano, 2015; Lu et al., 2017; Floyd and Lamy, 2019; Dai, Wang, and Inhester, 2020; Mierla et al., 2022) One example that we will return to in Section 3.3 is DeForest, de Koning, and Elliott (2017a), who used polarization data in STEREO-A COR2 coronagraph data to map the position of the front and core of a CME in three dimensions. When they reprojected it onto the plane of sky observed by the SOHO LASCO coronagraph, they found consistent cotemporal structures between the two longitudinally displaced satellites.

The concept of a superparticle is of course an idealized one, and any solar wind structure will have some extent along the line of sight. It is therefore useful

to consider exactly how the position extracted from polarization relates to the position of the center of mass of compact structures along the line of sight, in order to then investigate what might be diagnosed when mass is not so compact.

2.2.1. Center of Mass

In the case of the center of mass (COM) calculation for a distribution of density (n_e) along a line of sight, we are calculating,

$$s_{COM} = \frac{\int_s n_e(s, \varepsilon) \cdot s \cdot ds}{\int_s n_e(s, \varepsilon) \cdot ds} \quad (1)$$

where s is the distance along the line of sight from the Thomson Sphere (TS) to the scattering point. From Figure 1 we see that,

$$s = d \cdot \tan(\tau) \quad (2)$$

$$ds = \frac{d}{\cos^2(\tau)} d\tau \quad (3)$$

where d is the radius of closest approach of the line of sight, i.e., the intersection with the TS, and τ is the angle along the line of sight from this to each scattering point. Note that d can be directly related to the line-of-sight elongation angle ε and the observer's distance from the Sun. Taking observations from Earth, we have:

$$\begin{aligned} d &= r_{obs} \cdot \sin(\varepsilon) \\ &= 1 \text{ au} \cdot \sin(\varepsilon) \\ &= 215 R_{\odot} \cdot \sin(\varepsilon). \end{aligned} \quad (4)$$

So for a concentration of density at $\tau = \tau_o$,

$$s_{COM} = d \cdot \tan(\tau_o) \quad (5)$$

$$\tau_{COM} = \tau_o \quad (6)$$

2.2.2. Polarization Ratio

As shown in e.g., Guhathakurta (1989),

$$\begin{aligned} pB &\equiv B_T - B_R \\ &= \int_s \mathcal{G}_1 \cdot n_e(s, \varepsilon) \cdot ds \\ tB &\equiv B_T + B_R \\ &= \int_s (2 \cdot \mathcal{G}_2 - \mathcal{G}_1) \cdot n_e(s, \varepsilon) \cdot ds \end{aligned} \quad (7)$$

where B_R, B_T are radially and tangentially polarized light respectively, and

$$\begin{aligned}
\mathcal{G}_1(r, \chi) &= \mathcal{F}_o \cdot [(1-u) \cdot A(r) + u \cdot B(r)] \cdot \sin^2(\chi) \\
&= \mathcal{G}'_1(r) \cdot \sin^2(\chi) \\
\mathcal{G}_2(r) &= \mathcal{F}_o \cdot [(1-u) \cdot C(r) + u \cdot D(r)]
\end{aligned} \tag{8}$$

where

$$\mathcal{F}_o = \frac{\mathcal{C}_1}{(1 - \frac{u}{3})} \tag{9}$$

\mathcal{C}_1 is a constant, A, B, C, D are the standard radially-dependent van der Hulst coefficients of Thomson scattering, and u is the limb darkening coefficient.

So, the *degree of polarization* due to Thomson scattering of the K-corona, pB/tB , can be written as

$$p = \frac{\int_s \mathcal{G}'_1(r) \cdot \sin^2(\chi) \cdot n_e(s, \varepsilon) \cdot ds}{\int_s (2 \cdot \mathcal{G}_2(r) - \mathcal{G}'_1(r) \cdot \sin^2(\chi)) \cdot n_e(s, \varepsilon) \cdot ds} \tag{10}$$

and recalling that

$$\begin{aligned}
\sin^2(\chi) &= \cos^2(\tau) \\
s &= d \cdot \tan(\tau) \\
ds &= \frac{d}{\cos^2(\tau)} d\tau
\end{aligned}$$

we can express this in terms of line-of-sight angle, τ ,

$$p = \frac{\int_\tau \mathcal{G}'_1(r) \cdot n_e(\tau) \cdot d\tau}{\int_\tau (\frac{2\mathcal{G}_2(r)}{\cos^2(\tau)} - \mathcal{G}'_1(r)) \cdot n_e(\tau) \cdot d\tau} \tag{11}$$

For a superparticle positioned at $\tau = \tau_o$ with no other emission along a line of sight ε , the integrals may be ignored and the degree of polarization simplifies to:

$$\begin{aligned}
p &= \frac{\mathcal{G}'_1(r(\varepsilon, \tau_o)) \cdot n_e(\tau_o)}{(\frac{2\mathcal{G}_2(r(\varepsilon, \tau_o))}{\cos^2(\tau_o)} - \mathcal{G}'_1(r(\varepsilon, \tau_o))) \cdot n_e(\tau_o)} \\
&= \frac{\cos^2(\tau_o)}{(2 \cdot \frac{\mathcal{G}_2(r(\varepsilon, \tau_o))}{\mathcal{G}'_1(r(\varepsilon, \tau_o))} - \cos^2(\tau_o))}
\end{aligned} \tag{12}$$

We define the *polarization ratio* of radially to tangentially polarized light as,

$$PR \equiv \frac{B_R}{B_T} \quad (13)$$

$$= \frac{tB - pB}{tB + pB} \quad (14)$$

$$= \frac{1 - p}{1 + p} \quad (15)$$

$$= 1 - \frac{\mathcal{G}_2(r(\varepsilon, \tau_o))}{\mathcal{G}_1(r(\varepsilon, \tau_o))} \cdot \cos^2(\tau_o)$$

For everywhere except very close to the Sun, it can be shown that (see e.g. Howard and Tappin (2009); de Koning et al. (2025)) the van de Hulst coefficients become,

$$A = C = \frac{3}{2}B = \frac{3}{2}D = \mathcal{C}_2 r^{-2} \quad (16)$$

so $\mathcal{G}_2 = \mathcal{G}_1'$, and we can simplify further:

$$p = \frac{\cos^2(\tau_o)}{2 - \cos^2(\tau_o)} \quad (17)$$

$$PR = 1 - \cos^2(\tau_o) = \sin^2(\tau_o) \quad (18)$$

which matches the far-field formula derived by DeForest, Howard, and Tappin (2013b).

If we define an angular distance from the TS in terms of polarization ratio,

$$\tau_{pol} = \text{asin}(\sqrt{PR}) \quad (19)$$

For the δ -function mass distribution centered at $\tau = \tau_o$ (i.e., the superparticle that we have been discussing), this is simply

$$\tau_{pol} = |\tau_o| \quad (20)$$

τ_{pol} is unsigned and may arise from either of the two $\pm\tau_o$ solutions symmetric about the TS. The sign ambiguity is due to the asin function (the ambiguity in the square root is resolved by the geometry of the scattering plane – see Appendix B of DeForest et al. (2025) for discussion).

Similarly,

$$\begin{aligned} s_{pol} &= d \cdot \tan(\tau_{pol}) = d \cdot \frac{\sqrt{PR}}{\sqrt{1 - PR}} \\ &= r_{obs} \cdot \sin(\varepsilon) \cdot \frac{\sqrt{PR}}{\sqrt{1 - PR}} \end{aligned} \quad (21)$$

If $\tau_o = \tau_{pol} = 0$, meaning the superparticle is located at the TS, we see that $s_{pol} = PR = 0$, just as would be expected.

From Figure 1 we see that in general, $\pm s_{pol}$ can be related to two positions along the X -axis,

$$\begin{aligned}
x_{pol} &= d \cdot \sin(\varepsilon) \pm s_{pol} \cdot \cos(\varepsilon) \\
&= d \cdot \sin(\varepsilon) \pm d \cdot \cos(\varepsilon) \tan(|\tau_{pol}|) \\
&= r_{obs} \cdot \sin(\varepsilon) \cdot [\sin(\varepsilon) \pm \cos(\varepsilon) \tan(|\tau_{pol}|)] \\
&= r_{obs} \cdot \sin(\varepsilon) \cdot [\sin(\varepsilon) \pm \cos(\varepsilon) \frac{\sqrt{PR}}{\sqrt{1-PR}}] \tag{22}
\end{aligned}$$

Inspection of Figure 1 shows us that the complete three-dimensional location of the superparticle can be specified in Cartesian coordinates from Equations 22 and

$$y_{pol} = (r_{pos} - x_{pol} \cdot \tan(\varepsilon)) \cdot \sin(\alpha) \tag{23}$$

$$z_{pol} = (r_{pos} - x_{pol} \cdot \tan(\varepsilon)) \cdot \cos(\alpha) \tag{24}$$

In summary: if sufficiently compact (more on this in Section 2.5), we can directly relate PUNCH observations of pB , tB to the 3D COM position of a superparticle — subject to a sign ambiguity as to whether it is in front or behind the TS (see Section 3.2). Once this ambiguity is resolved, the 3D position of the superparticle is obtained.

2.3. Diagnosing Radial Density Falloff

The density falloff in the background corona and solar wind is generally radial, i.e., $n_e \propto r^{-c}$ (Saito et al., 1970), with density exponent c decreasing from values of order 10 to 20 in the very low corona (Gibson et al., 1999; Guhathakurta et al., 1999) where wind flow is subsonic and scale height effects dominate, to the asymptotic value of 2 expected for a constant-velocity solar wind in interplanetary space (Parker, 1957). We note that the fast solar wind is expected to reach its final speed closer to the Sun than the slow solar wind, which continues to accelerate to large distances so that $c > 2$ (Bunting et al., 2024). For the range of distances relevant to PUNCH that we primarily consider in this paper, the expected range of variation in c is between 2 and 4, e.g., as shown in the observationally-constrained model of Leblanc, Dulk, and Bougeret (1998), $c \approx 3.35$ at $r = 5 R_{\odot}$, and it decreases to 2.30 at $r = 10 R_{\odot}$, then to 2.002 at $r = 100 R_{\odot}$. Using data from *Parker Solar Probe*, Maruca et al. (2023) found evidence for solar wind acceleration between 30 and 150 R_{\odot} , with an associated density exponent $c \approx 2.26$ in that region. One-dimensional turbulence-driven models provide similar ranges, with the full set of ZEPHYR models from Cranmer, van Ballegoijen, and Edgar (2007) and Cranmer, van Ballegoijen, and Woolsey (2013) having median values of c of 2.97, 2.47, and 2.07 at $r = 5, 10$, and 100 R_{\odot} , respectively.

Fitting the exponent c to observations has generally required measurements at multiple radial heights in order to measure the slope of the density falloff. As

we will now show, the polarization ratio PR provides a direct, local measurement of this global property. As a parallel with the superparticle analysis, we again consider the relation between COM and the diagnostic provided from white light polarization data.

2.3.1. Center of Mass

Consider a spherically symmetric density falloff,

$$n_e(r) = n_o \cdot r^{-c} \quad (25)$$

Combining this with Equations 1 - 3 and using

$$r = \frac{d}{\cos(\tau)} \quad (26)$$

we find for each line of sight of a given elongation angle, ε ,

$$s_{COM}(\varepsilon) = \frac{d(\varepsilon) \cdot \int_{\tau_-}^{\tau_+} \sin(\tau) \cdot \cos^{c-3}(\tau) \cdot d\tau}{\int_{\tau_-}^{\tau_+} \cos^{c-2}(\tau) \cdot d\tau}. \quad (27)$$

Taking as an example the spherically expanding constant speed solar wind case, $c = 2$, it follows that

$$s_{COM}(\varepsilon) = \frac{d(\varepsilon) \cdot [\ln(\cos(\tau_-)) - \ln(\cos(\tau_+))]}{\tau_+ - \tau_-} \quad (28)$$

For such a distribution of spherically symmetric density falling off with distance, $n_e(\tau)$ peaks at the TS ($s = \tau = 0$) for each line of sight. Thus, Equation 28 returns a value of zero for lines of sight that are symmetric about the TS, i.e., $\tau_+ = -\tau_-$.

However, in solving the integrals for such extended distributions, it is essential to address the inherent asymmetry of lines of sight about the TS. From Figure 1 we see that in general, lines of sight coming from the observer will have limits of integration $\tau_+ = \frac{\pi}{2} - \varepsilon$, $\tau_- = -\frac{\pi}{2}$, so for the $c = 2$ example,

$$s_{COM}(\varepsilon) = d(\varepsilon) \cdot \frac{1}{\pi - \varepsilon} \cdot (\ln[\cos(\frac{\pi}{2})] - \ln[\cos(\frac{\pi}{2} - \varepsilon)]) \quad (29)$$

$$= \frac{r_{obs}}{\pi - \varepsilon} \cdot \sin(\varepsilon) \cdot (-\infty - \sin(\varepsilon)) \quad (30)$$

The general solution for the asymmetric case, for lines of sight $0 < \varepsilon < \frac{\pi}{2}$, is:

$$s_{COM} = -\infty \quad (31)$$

$$\tau_{COM} = -\frac{\pi}{2} \quad (32)$$

2.3.2. Polarization Ratio

The τ_{pol} calculated from the polarization ratio using Equation 19 no longer diagnoses the COM for such extended distributions. Instead, it diagnoses the radial falloff of density, as we now describe.

As already noted, we can simplify by assuming the scattering occurs far enough from the Sun for it to be considered a point source (true for the PUNCH FOV $> 5R_{\odot}$). In that limit of large r , it follows from Equations 8-9 and 16 that

$$\mathcal{G}_2 = \mathcal{G}'_1 = \mathcal{C}_1 \cdot \left(\frac{1}{6}\right) \cdot \mathcal{C}_2 \cdot r^{-2} \quad (33)$$

Equation 11 becomes,

$$p = \frac{\int r^{-2} \cdot n_e(\tau) \cdot d\tau}{\int r^{-2} \cdot n_e(\tau) \cdot (2\sec^2(\tau) - 1) \cdot d\tau} \quad (34)$$

For the spherically symmetric falloff $n_e(r) = n_o \cdot r^{-c}$, again using $r = \frac{d}{\cos(\tau)}$ and adding limits of integration along an observer's lines of sight ε , it follows that,

$$p = \frac{\int_{\tau_-}^{\tau_+} \cos^q(\tau) \cdot d\tau}{\int_{\tau_-}^{\tau_+} 2 \cos^{(q-2)}(\tau) - \cos^q(\tau) \cdot d\tau} \quad (35)$$

where $q = c + 2$.

From Gradshteyn and Ryzhik (2007) we see that, for $q > 0$,

$$\begin{aligned} \int_{\tau_-}^{\tau_+} \cos^q(\tau) \cdot d\tau &= \frac{\cos^{q-1}(\tau_+) \cdot \sin(\tau_+)}{q} \\ &\quad - \frac{\cos^{q-1}(\tau_-) \cdot \sin(\tau_-)}{q} \\ &\quad + \frac{q-1}{q} \int_{\tau_-}^{\tau_+} \cos^{q-2}(\tau) \cdot d\tau \end{aligned} \quad (36)$$

Integrating from $\tau_- = -\frac{\pi}{2}$ to $\tau_+ = \frac{\pi}{2}$, this reduces to

$$\int_{-\frac{\pi}{2}}^{\frac{\pi}{2}} \cos^q(\tau) \cdot d\tau = \frac{q-1}{q} \int_{-\frac{\pi}{2}}^{\frac{\pi}{2}} \cos^{q-2}(\tau) \cdot d\tau \quad (37)$$

so Equation 35 becomes

$$\begin{aligned}
p_{symm} &= \frac{\frac{q-1}{q} \int_{-\frac{\pi}{2}}^{\frac{\pi}{2}} \cos^{q-2}(\tau) \cdot d\tau}{\int_{-\frac{\pi}{2}}^{\frac{\pi}{2}} 2 \cos^{q-2}(\tau) - \frac{q-1}{q} \int_{-\frac{\pi}{2}}^{\frac{\pi}{2}} \cos^{q-2}(\tau) \cdot d\tau} \\
&= \frac{1}{2 \frac{q}{q-1} - 1} \\
&= \frac{q-1}{2q - q + 1} \\
&= \frac{q-1}{q+1} \\
&= \frac{c+1}{c+3}
\end{aligned} \tag{38}$$

We note that Equation 38 was first presented in this form by Saito et al. (1970), with related expressions found in work referenced therein, i.e., Schuster (1879) and Baumbach (1938).

From this we see that

$$\begin{aligned}
PR_{symm} &= \frac{1 - p_{symm}}{1 + p_{symm}} \\
&= \frac{1}{c+2}
\end{aligned} \tag{39}$$

If we calculate τ_{pol} for such a symmetric distribution, we find that

$$\tau_{pol_{symm}} = \text{asin}(\sqrt{PR_{symm}}) = \text{asin}\left(\sqrt{\frac{1}{c+2}}\right) \tag{40}$$

Equation 40 is analogous to Equation 20, but conceptually represents a radically different diagnostic. The latter is a diagnostic of position along the line of sight for a superparticle, while the former is a diagnostic of density slope for a radially-symmetric expanding solar wind.

To establish how generally this slope diagnostic might be used, we need to consider the effects of asymmetric integration limits for lines of sight $\varepsilon > 0$. In these cases, we see from Equation 37 that an additional correction term dependent on line-of-sight elongation angle ε needs to be added:

$$F_{corr}(\varepsilon) = \frac{\sin^{q-1}(\varepsilon) \cdot \cos(\varepsilon)}{q} \tag{41}$$

This leads us to the general (solar point-source) asymmetric solution,

$$p = \frac{\frac{q-1}{q} \int_{-\frac{\pi}{2}}^{\frac{\pi}{2}-\varepsilon} \cos^{q-2}(\tau) \cdot d\tau + F_{corr}(\varepsilon)}{\int_{-\frac{\pi}{2}}^{\frac{\pi}{2}-\varepsilon} 2 \cos^{q-2}(\tau) \cdot d\tau - \frac{q-1}{q} \int_{-\frac{\pi}{2}}^{\frac{\pi}{2}-\varepsilon} \cos^{q-2}(\tau) \cdot d\tau - F_{corr}(\varepsilon)} \tag{42}$$

It is clear that as $\varepsilon \rightarrow 0$, $F_{corr}(\varepsilon) \rightarrow 0$, and similarly as $\varepsilon \rightarrow \frac{\pi}{2}$, $F_{corr}(\varepsilon) \rightarrow 0$. For both of these limits, the symmetric solutions Equations 38-40 are regained.

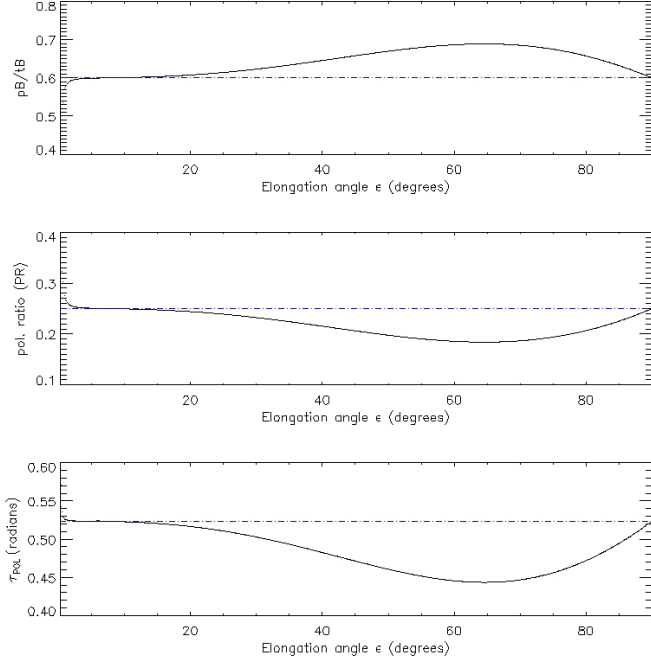


Figure 2. Diagnostics obtained for a density distribution $n_e(r) = n_o \cdot r^{-2}$. Top: Ratio of white-light polarized brightness to total brightness (p), middle: polarization ratio (PR), and bottom: τ_{pol} , all plotted vs elongation angle ϵ . The blue dash-dotted line shows the asymptotically regained symmetric solutions, $p_{symm} = 3/5$, $PR_{symm} = 1/4$, and $\tau_{pol_{symm}} = \text{asin}(\sqrt{1/4})$. Differences are seen between this simplified point-source solution and the solid-black-line complete-form solution, which takes into account the extended disk of the Sun and truncates lines of sight at the observer, as discussed in the text.

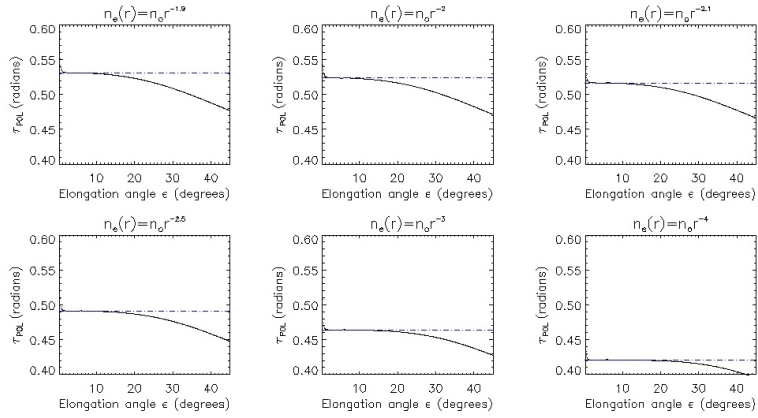


Figure 3. Forward modeled τ_{pol} for $n_e = r^{-c}$ spherically symmetric density distributions, for choices of (top) $c = 1.9, 2.1, 2.2$ and (bottom) $c = 2.5, 3, 4$, for elongation angles $\epsilon < 45^\circ$.

To demonstrate this, we again consider the case of $q = 4, c = 2, n_e = n_o \cdot r^{-2}$. In this case, Equation 42 becomes

$$\begin{aligned}
 p &= \frac{\frac{1}{4}[\int_{-\frac{\pi}{2}}^{\frac{\pi}{2}-\varepsilon} 3 \cos^2(\tau) \cdot d\tau + \sin^3(\varepsilon) \cdot \cos(\varepsilon)]}{\frac{1}{4}[\int_{-\frac{\pi}{2}}^{\frac{\pi}{2}-\varepsilon} 5 \cos^2(\tau) \cdot d\tau - \sin^3(\varepsilon) \cdot \cos(\varepsilon)]} \\
 &= \frac{3(\frac{\pi-\varepsilon}{2} + \frac{1}{4} \sin(\pi - 2\varepsilon)) + \sin^3(\varepsilon) \cdot \cos(\varepsilon)}{5(\frac{\pi-\varepsilon}{2} + \frac{1}{4} \sin(\pi - 2\varepsilon)) - \sin^3(\varepsilon) \cdot \cos(\varepsilon)} \\
 &= \frac{3}{5}(\varepsilon \rightarrow 0)
 \end{aligned}$$

Figure 2 shows the quantities p, PR, τ_{pol} for the $n(r) = n_o \cdot r^{-2}$ falloff, using the complete form Equation 11 (that is, not assuming a solar point source). As expected, the symmetric solutions are regained as $\varepsilon \rightarrow \frac{\pi}{2}(90^\circ)$. As $\varepsilon \rightarrow 0$, the complete solution (black line) diverges from the point-source solution due to the proximity to the solar disk (see Equation 8 and van de Hulst (1950)). Figure 3 shows how polarization would change for various choices of slope c in the PUNCH field of view, $\varepsilon = 0 - 45^\circ$. In general, the departure from the symmetric, simplified solution is minor for ($\varepsilon < 15^\circ$), indicating it should be possible to distinguish between these slopes.

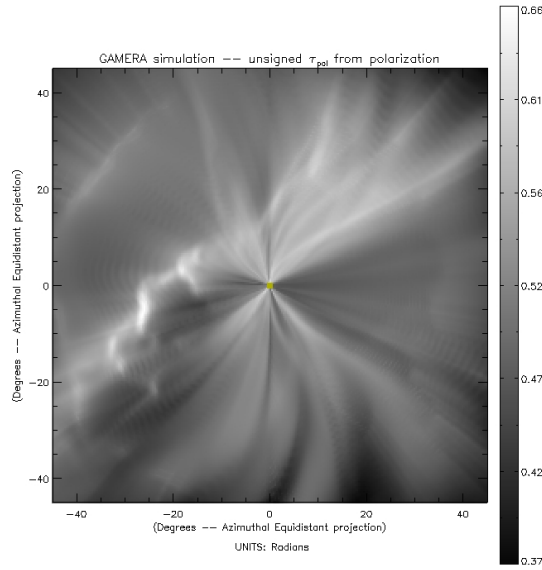


Figure 4. Forward-modeled τ_{pol} for a global solar wind simulation obtained by GAMERA-Helio model of the solar wind driven by the Wang-Sheeley-Arge Air Force Data Assimilative Photospheric Flux Transport (WSA/ADAPT) model output for Carrington rotation 2065 (Provornikova et al., 2024). The background (non-structured) solar wind has a non-zero value, consistent with a radially-falling off density, as discussed in the text.

Something close to a r^{-2} falloff is what we would expect to see for a mass-conserving constant-speed solar wind, and indeed, Figure 4 shows $\tau_{pol_{r^{-2}}} =$

$\text{asin}(\sqrt{1/4}) = 0.524$ is the central value from a global simulation of a forward-modeled complex solar wind (also seen in Figures 2 and 3).

In summary: For observations along lines of sights with elongation angles in the range $\sim 1 - 15^\circ$, PUNCH white light polarization observations will provide a local diagnostic of density radial falloff for the background solar wind, independent from and complementary to non-local techniques. The effects of asymmetry are predictable and small enough to distinguish between falloff slopes in the lower part of the PUNCH/NFI field of view ($2 - 10r_\odot^1$).

2.4. Transitioning from compact to distributed

It is instructive to consider how τ_{pol} varies for a wedge of constant density centered on τ_o as it increases its line-of-sight (LOS) linear width w . Note that de Koning et al. (2025) uses a similar approach, but considers features with angular half-width Δ symmetric about τ_o (rather than linear half-width $\frac{w}{2}$ symmetric about τ_o), and lets density vary as r^{-2} ($c = 2$) in order to probe how polarization diagnostics apply to 2D sheet-like structures associated with SIRs. Our purpose in this section is somewhat different. We consider wedges of constant density ($c = 0$) and vary linear width to calculate the polarization ratio at two extremes – i.e., delta-function vs infinitely-extended wedge ($w \rightarrow \infty$). The latter is obviously unrealistic, but it allows us to show the transition between the polarization diagnostics described in Section 2.2 (appropriate to a 0D, or 1D caustic collection of points) and Section 2.3 (appropriate for an infinitely-extended 3D distribution of density). It will also allow us to consider the conditions under which these limits apply for a structure centered on τ_o (Section 2.5). As above, we pay special attention to the significance of asymmetries introduced by the observer’s position truncating the line of sight.

2.4.1. Center of Mass

The COM transition from compact to infinitely extended masses is trivial for the symmetric case (ignoring the observer), as might be expected from our discussions in Sections 2.2.1 and 2.3.1. Figure 5 (left) illustrates the constant density case ($c = 0$), which for the symmetric integration (blue line) results in $\tau_{COM} = \tau_o$ for all LOS half-widths. For the asymmetric solution (taking the observer’s position into account; red line), the solution approaches $\tau_{COM} = -\frac{\pi}{2}$ ($= 90^\circ$) as in Equation 32. The departure from the symmetric solution occurs as soon as the wedge LOS half-width $\frac{w}{2}$ reaches the distance from the TS to the observer,

$$s_{+limit} = r_{obs}(\cos(\varepsilon) - \sin(\varepsilon) \tan(\tau_o)) \quad (43)$$

This position is indicated by the vertical yellow line.

¹Note throughout this paper we use the r_\odot to signify the fixed solar radius, $r_\odot = 695700 \text{ km}$. This is not to be confused with the unit R_\odot sometimes used in DeForest et al. (2025) and other PUNCH papers, which is a convenience unit defined as the approximate apparent solar radius in elongation angle ε when viewed from $1au$, i.e., $R_\odot = 0.25^\circ$.

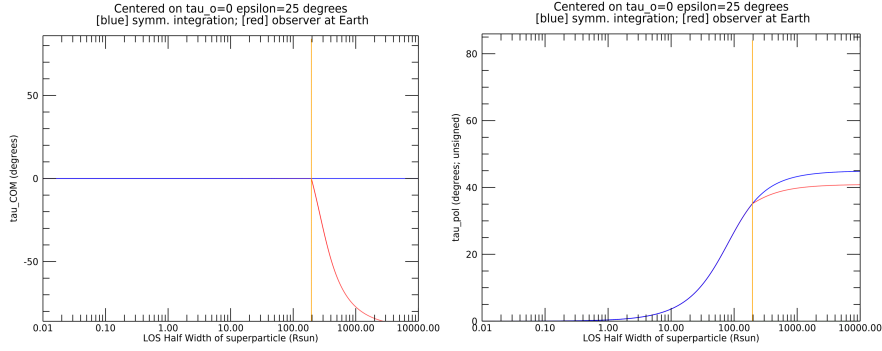


Figure 5. (Left) Center of mass angular position τ_{COM} for a constant-density wedge of varying LOS linear half-width $\frac{w}{2}$, centered on the Thomson Sphere ($\tau_o = 0$), at line-of-sight elongation angle $\varepsilon = 25^\circ$. (Right) Unsigned τ_{pol} determined from the polarization ratio (PR) as a function of wedge half-width, which reproduces $\tau_{COM} = \tau_o = 0^\circ$ for small LOS widths and asymptotes to 45° for the infinite wedge as described in the text. The blue lines are the symmetric solution integrated from $-\frac{w}{2}$ to $\frac{w}{2}$, while the red lines are the asymmetric solutions integrated from $-\frac{w}{2}$ to $\frac{w}{2} < s_{+limit}$, defined in Equation 43. The vertical orange lines are placed at s_{+limit} (see text).

2.4.2. Polarization Ratio

The question of how polarization diagnostics vary with increasing LOS half-width $\frac{w}{2}$ has clear observational significance. The constant density $c = 0, q = 2$ case of Equation 35 gives us

$$p = \frac{\int_{\tau_-}^{\tau_+} \cos^2(\tau) d\tau}{\int_{\tau_-}^{\tau_+} 2 - \cos^2(\tau) d\tau} \quad (44)$$

and

$$\begin{aligned} PR &= \frac{\int_{\tau_-}^{\tau_+} \sin^2(\tau) d\tau}{\int_{\tau_-}^{\tau_+} d\tau} \\ &= \frac{1}{2} \cdot \left[1 - \frac{\sin(2\tau_+) - \sin(2\tau_-)}{2(\tau_+ - \tau_-)} \right] \end{aligned} \quad (45)$$

leading us to the general equation,

$$\tau_{pol} = \text{asin}\left(\sqrt{\frac{1}{2} \cdot \left(1 - \frac{\sin(2\tau_+) - \sin(2\tau_-)}{2(\tau_+ - \tau_-)}\right)}\right) \quad (46)$$

where for the symmetric case,

$$\tau_{\pm} = \text{atan}\left(\frac{s_{\pm}}{d}\right) = \text{atan}\left(\tan(\tau_o) \pm \frac{w}{2d}\right) \quad (47)$$

Recalling that $d = r_{obs} \sin(\varepsilon)$, and that $r_{obs} = 215R_{\odot}$ and $1.5^\circ < \varepsilon < 45^\circ$ in the PUNCH field of view, it is immediately clear that if $\frac{w}{2d} \gg \tan(\tau_o)$, Equation 47 loses sensitivity to τ_o , and τ_{\pm} go to $\pm \frac{\pi}{2}$. τ_{pol} thus achieves its

asymptotic value of $\frac{\pi}{4} = 45^\circ$, as expected from Equation 40 for an infinitely extended, uniform density distribution, $c = 0$. This is seen in the right panel of Figure 5, which shows the case of $\tau_o = 0$ (wedge centered on the TS) and $\varepsilon = 25^\circ$. It is generally true for all choices of τ_o and ε in the large LOS width (symmetric) limit, as shown in Figure 6.

The asymmetric case (red lines in Figures 5 and 6) truncates the integral at the observer,

$$\begin{aligned}
\tau_{+limit} &= \text{atan}\left(\frac{s_{+limit}}{r_{obs} \sin(\varepsilon)}\right) \\
&= \text{atan}\left(\frac{r_{obs}[\cos(\varepsilon) - \sin(\varepsilon) \tan(\tau_o)]}{r_{obs} \sin(\varepsilon)}\right) \\
&= \text{atan}\left(\frac{1}{\tan} \varepsilon - \tan(\tau_o)\right) \\
&= \frac{\pi}{2} - \varepsilon
\end{aligned} \tag{48}$$

which for the $\varepsilon = 25^\circ$ case shown in Figure 5 results in $\tau_{+limit} = 65^\circ$ and an asymptotic approach to

$$\begin{aligned}
\tau_{pol} &= \pm \text{asin}\left[\sqrt{\frac{1}{2} \cdot \left(1 - \frac{\sin(\frac{13\pi}{18}) + \sin(\pi)}{(\frac{13\pi}{18} + \pi)}\right)}\right] \\
&= 0.714 = 40.93^\circ
\end{aligned} \tag{49}$$

It is interesting to compare the top left ($\varepsilon = 1^\circ, \tau_o = 0^\circ$) and bottom right ($\varepsilon = 89^\circ, \tau_o = 0^\circ$) panels of Figure 6, which both show minimal difference between the symmetric (blue) and asymmetric (red) solution – but for different reasons. In the case of $\varepsilon = 1^\circ$, lines of sight are essentially parallel so that the solution is intrinsically symmetric, while for the case of $\varepsilon = 89^\circ$, the observer is at $\tau_{+limit} = 1^\circ$ and the line of sight lies almost entirely outside the Thomson Sphere, $\tau > 0$, such that the solution is intrinsically asymmetric.

To recover the superparticle approximation, we apply a first order Taylor expansion about $\tan(\tau_o)$ for small $\frac{w}{2d}$ to Equation 47.

$$\begin{aligned}
\tau_{\pm} &\rightarrow \tau_o \pm \frac{w}{2d} \cos^2 \tau_o \\
\sin(2\tau_+) - \sin(2\tau_-) &\rightarrow 2 \cos(2\tau_o) \sin\left(\frac{w}{d} \cos^2 \tau_o\right) \\
2\tau_+ - 2\tau_- &\rightarrow 2 \frac{w}{d} \cos^2 \tau_o
\end{aligned}$$

Then Equation 46 reduces to a small-width form,

$$\tau_{pol} \rightarrow \text{asin}\left(\sqrt{\frac{1}{2} \cdot \left(1 - \cos(2\tau_o) \frac{\sin(\frac{w}{d} \cos^2 \tau_o)}{\frac{w}{d} \cos^2 \tau_o}\right)}\right) \tag{50}$$

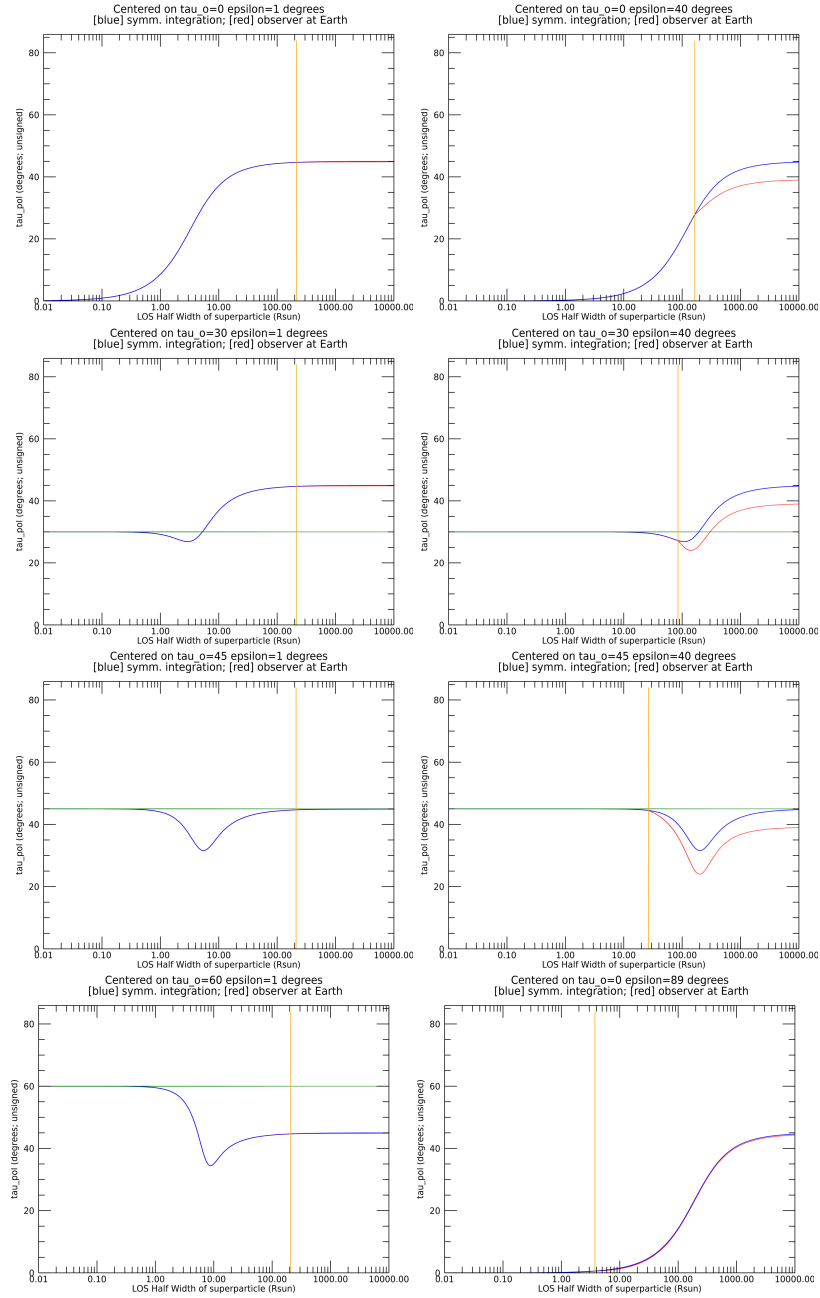


Figure 6. Polarization ratio angular position τ_{pol} as in Figure 5 (right) for (left column) $\epsilon = 1^\circ$ ($\tau_o = 0, 30, 45, 60^\circ$), (right column top three panels) $\epsilon = 40^\circ$ ($\tau_o = 0, 30, 45^\circ$), and (bottom right) $\epsilon = 89^\circ$ ($\tau_o = 0^\circ$). Note that we avoid combinations of τ_o and ϵ that would center the wedge behind the observer due to $\tau_o + \epsilon > 90^\circ$. Vertical lines are as described in Figure 5, and horizontal line is placed at wedge center τ_o .

In the limit $\frac{w}{d} \cos^2 \tau_o \rightarrow 0$,

$$\begin{aligned}
\tau_{pol} &= \text{asin}\left(\sqrt{\frac{1}{2} \cdot (1 - \cos(2\tau_o))}\right) \\
&= \text{asin}\left(\sqrt{\sin^2(\tau_o)}\right) \\
&= |\tau_o|
\end{aligned} \tag{51}$$

This is a general result, and when achieved by LOS width $\rightarrow 0$, it is independent of τ_o and ε (see Figure 6). We note in passing $\tau_{pol} = |\tau_o|$ is achieved exactly when $|\tau_o| = 90^\circ$, which is of academic interest only as it involves a wedge placed at infinity. It is however significant that there is a dependency on τ_o – and through d , on ε – that needs to be considered when determining how small the linear LOS widths must be to be considered “localized”, as we will discuss in the next section.

In summary, by considering varying linear LOS-width wedges of constant density centered at angular distance τ_o from the TS, we have demonstrated the transition from a superparticle solution to the spherically-symmetric density solution extended infinitely along the line of sight, with adjustment for asymmetric lines of sight that truncate at the observer’s position.

2.5. Defining “localization”: Quantifying errors and understanding limitations on superparticle analysis

We have demonstrated that the polarization analysis returns “truth” for the wedge center position, i.e., $\tau_{pol} = |\tau_o|$, for wedge LOS widths $\frac{w}{d} \cos^2(\tau_o) \ll 1$. In this small width limit, the angular half-width considered in the treatment of de Koning et al. (2025) can be expressed as $\Delta \approx \frac{w}{2d} \cos^2 \tau_o$ and will be symmetric about τ_o (not generally true, as we define τ_o as the center of the linear width w as opposed to the center of angular width 2Δ). Indeed the small-width limit found in de Koning et al. (2025) for a constant density model, $2\Delta \ll 1$, is equivalent to our requirement $\frac{w}{d} \cos^2(\tau_o) \ll 1$. Structures meeting this condition can thus be said to be localized – subject to an error that is maximum (in the small-width limit) when the wedge straddles the TS, which we now quantify.

For the case shown in Figure 5, $\tau_o = 0$ and $\tau_{\pm} = \pm \text{atan}(\frac{w}{2d})$. Since

$$\begin{aligned}
\sin(2 \text{atan}(\frac{w}{2d})) &= 2 \sin(\text{atan}(\frac{w}{2d})) \cos(\text{atan}(\frac{w}{2d})) \\
&= \frac{\frac{w}{d}}{1 + (\frac{w}{2d})^2}
\end{aligned}$$

Equation 46 at the TS then is,

$$\tau_{polTS} = \text{asin}\left(\sqrt{\frac{1}{2} \cdot \left[1 - \frac{\frac{w}{2d}}{\text{atan}(\frac{w}{2d})[1 + (\frac{w}{2d})^2]}\right]}\right) \tag{52}$$

Equation 52 quantifies the error on the solution of $\tau_{pol} = \tau_o = 0$ at the TS, an error that approaches zero as $\frac{w}{2d} \rightarrow 0$ and 45° as $\frac{w}{2d} \rightarrow \infty$. The general form of this error, $\tau_{diff} = \tau_{pol} - |\tau_o|$, is calculated numerically from Equations 46

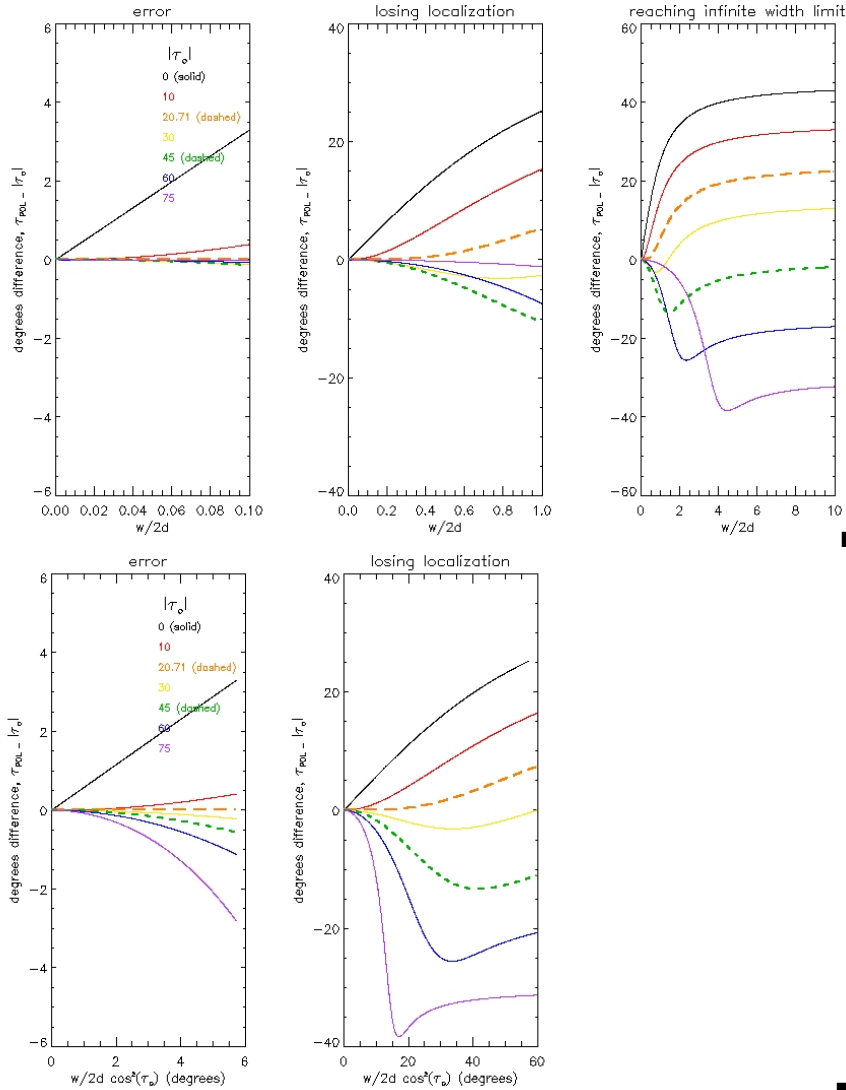


Figure 7. $\tau_{diff} = \tau_{pol} - |\tau_o|$ plotted vs (top) linear half-width $\frac{w}{2d}$ and (bottom) $\frac{w}{2d} \cos^2(\tau_o)$ (which is the angular half-width Δ in the small-width limit). The bottom panels have the same horizontal axis range as the top panels, expressed in degrees rather than radians. The solid black line is for a wedge centered on the TS, $\tau_o = 0^\circ$, and the colored lines represent different choices of $|\tau_o|$ (shown in degrees in the left panel text inset). Panels show results for the small-width regime (left), the middle-width regime (middle), and the large-width (wedge size $\rightarrow \infty$) regime. All of the initial choices of wedge center τ_o result in τ_{diff} (the value being plotted) asymptoting to $45^\circ - \tau_o$ in this large-width limit.

and 47 and plotted for different choices of τ_o in Figure 7 as a function of linear half-width $\frac{w}{2d}$ (top panels) and small-width-limit angular half-width $\frac{w}{2d} \cos^2 \tau_o$ (left and middle bottom panels only where $\frac{w}{2d} \cos^2 \tau_o \leq 1$ (radians)). By utilizing the dimensionless parameters $\frac{w}{2d}$ and $\frac{w}{2d} \cos^2 \tau_o$, we remove dependence on ε .

The top left panel shows the small-width regime, and we see that the $\tau_o = 0^\circ$ case (black line) has a significantly larger error than wedges of the same linear width placed at different τ_o (colored lines), reaching $> 3^\circ$ at $\frac{w}{2d} = 0.1$. The bottom left panel makes the comparison for wedges with the same angular width as the TS-centered wedge, still in the small-width regime. The $|\tau_o| = 20.71^\circ$ line (dashed orange) represents a small-width minimum solution of τ_{diff} and lies tangent to the zero error line until $\frac{w}{2d} \approx 0.4$ or $\frac{w}{2d} \cos^2 \tau_o \approx 23^\circ$ (as seen in middle panels). For $|\tau_o| > 20.71^\circ$, $|\tau_{diff}|$ is negative. The middle panels show the small-width localization being lost and the top right panel shows the asymptotic infinite-width limit being reached for all choices of $|\tau_o|$.

Although there are zero crossings for $20.71^\circ < |\tau_o| < 45^\circ$ (e.g., the $|\tau_o| = 30^\circ$ yellow line), they *should not be taken as localization*. Rather, they are showing the transition toward the infinite-width solution $\tau_{pol} = 45^\circ$, which is the asymptotic

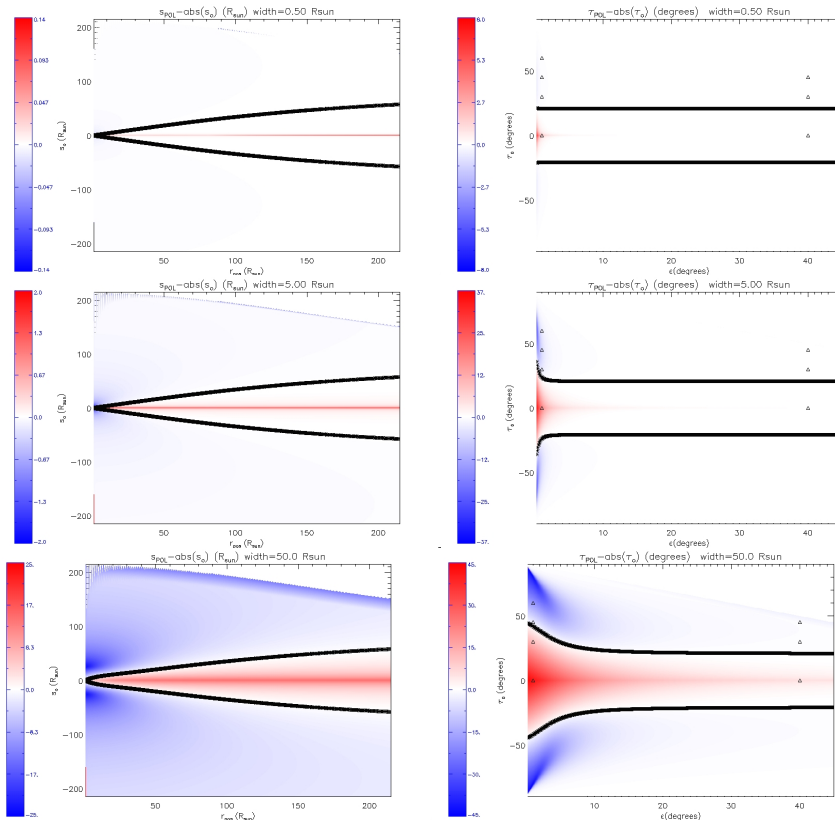


Figure 8. Color contours in the left column show the difference between s_{pol} and wedge center linear position s_o in r_\odot as a function of s_o (vertical) and r_{pos} (horizontal) for linear LOS widths of $w = 0.05, 0.5, 5.0r_\odot$ (top to bottom). Right column shows the same, but with color contours showing τ_{diff} in degrees as a function of τ_o (vertical) and ϵ (horizontal). The asymmetry for positive vs negative s_o, τ_o (seen in the bottom panels) is due to the requirement that the wedge lie between the TS and the Observer, $\tau_o \leq 90^\circ - \epsilon$. Triangles on the right-hand plots correspond to the choices of τ_o, ϵ shown in Figure 6. The solid black lines are solutions to $\tau_{diff} = \tau_{pol} - |\tau_o| = 0$ as discussed in the text.

behavior for all choices of τ_o as seen in the top right-hand panel of Figure 7 (45° needs to be subtracted from the absolute value of τ_o of each colored line to see this). The green dashed line is the case $|\tau_o| = 45^\circ$, which in the small-width limit is localized, but in the large-width limit achieves $\tau_{diff} = 0$ essentially by the coincidence of being centered on the value associated with an infinite-width wedge. This nonlinearity means that the τ_{diff} “error” on τ_{POL} is only generally meaningful in the small-width regime.

Figure 8 shows how τ_{diff} and the related linear position difference $s_{diff} = s_{pol} - |s_o|$ vary across the two dimensional (τ_o, ϵ) space, or equivalently (s_o, r_{pos}) space, for a choice of $w = 0.5, 5, 50r_\odot$ (top to bottom). For this we have drawn inspiration from Bemporad and Pagano (2015), who used similar plots to discuss polarization uncertainties close to the Sun.

For the smallest linear LOS width of $w = 0.5r_\odot$ (top panels), the difference is generally very small (appearing white). An exception is near $s_o = 0$ (left panel) or equivalently $\tau_o = 0$ and small ϵ (right panel), where the $\tau_{pol_{TS}}$ error of Equation 52 manifests. (We note that Bemporad and Pagano (2015) referred to this error as a “folding” effect of the unsigned contributions to the polarization ratio across the TS – mathematically contained in the $\cos^2 \tau_o$ term of Equation 50.) For example, for the minimum $\epsilon = 0.2665^\circ$ shown in the plot ($r_{pos} = d = 1R_\odot$), $\frac{w}{2d} = 0.25$ and $\tau_{diff} = \tau_{pol_{TS}} = 8.1^\circ$ at the TS. This corresponds to $s_{diff} = d \tan(\tau_{diff}) = 0.14R_\odot$, a little more than a quarter of the assumed wedge LOS width of $0.5r_\odot$. For larger values of $\epsilon(r_{pos})$, $\frac{w}{2d}$ and so the angular-width error τ_{diff} decreases, although the linear-width error s_{diff} at the TS is maintained farther due to its dependency on d and so $\sin(\epsilon)$. $\tau_{diff} = 0$ is indicated by the thick black lines, which intersect the left-hand vertical axis in the top right-hand panel at 21.22° (just above the small $\frac{w}{2d}$ limit of $\tau_o = \pm 20.705^\circ$, see Figure 7), corresponding to $s_o = \pm 0.39r_\odot$ in the top left-hand panel.

The middle panel value of $w = 5r_\odot$ is similar to that assumed by Bemporad and Pagano (2015), and indeed we get essentially identical results to them in the near-Sun, small- ϵ regime. At $\tau_o = 0$ and the minimum possible $\epsilon = 0.2665^\circ$ ($r_{pos} = d = 1r_\odot$), $\frac{w}{2d} = 2.5$, $\tau_{diff} = \tau_{pol_{TS}} = 36.6^\circ$, and $s_{diff} = d \cdot \tan(\tau_{diff}) = 0.74R_\odot$. The thick black line indicating $\tau_{diff} = 0$ reaches a value of $\tau_o = \pm 36.1^\circ$ or $s_o = \pm 0.73r_\odot$ at the (left-hand) vertical axis.

As the wedge LOS width gets larger still (bottom panels), negative and positive discrepancies grow, consistent with the transition to the infinite-wedge solution. In their near-Sun, small- ϵ regime (left-hand sides), the bottom plots have reached this limit, with maximum/minimum values $\tau_{diff} = \pm 45^\circ$ and the black $\tau_{diff} = 0$ line occurring as expected at $\tau_o = 45^\circ$ and $s_o = 1r_\odot$ as $\epsilon \rightarrow 0$. As discussed above, the black lines $\tau_{diff} = 0$ should not be taken as indicators of localization, i.e., “success” of the polarization diagnostic in reproducing the location of the wedge center. They occur where τ_o happens to coincide with τ_{pol} for a given $\frac{w}{2d}$ (see Figure 7). True success occurs in the parts of the plots that fade to white for all values of τ_o, s_o (other than the TS), i.e., where large ϵ drives $\frac{w}{2d} \ll 1$ as on the right-hand sides of Figure 8 panels.

Figure 9 removes the dependence on ϵ , as was done in Figure 7, by allowing LOS widths to vary as a fixed multiple of the linear LOS half-width parameter $\frac{w}{2d}$. This simplifies the problem greatly, and shows (top panel) how wedges with

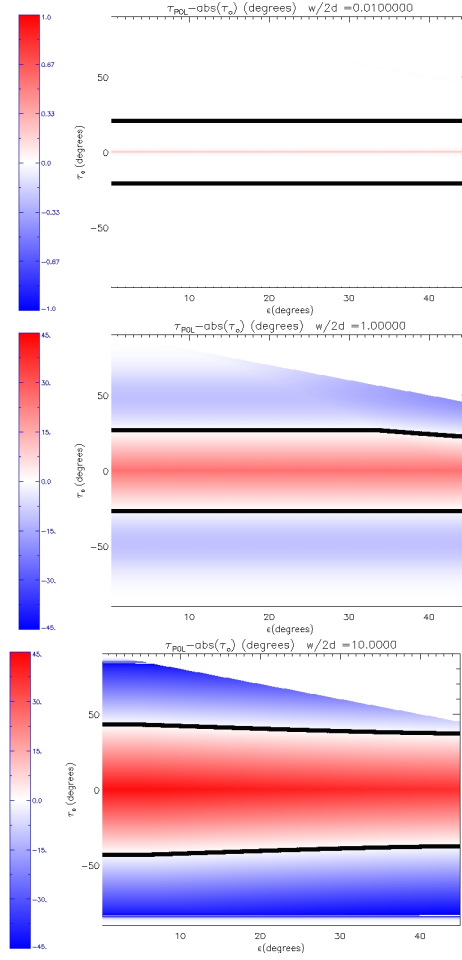


Figure 9. Color contours show $\tau_{diff} = \tau_{pol} - |\tau_o|$ as in Figure 8 (right column) for choices of $\frac{w}{2d} = 0.01$ (top), $\frac{w}{2d} = 1.0$ (middle), and $\frac{w}{2d} = 10.0$ (bottom). Black lines are solutions to $\tau_{diff} = 0$, appearing at $|\tau_o| = 20.705^\circ$ in the top panel, and approaching maximum $|\tau_o| = 45^\circ$ by the bottom panels. As in Figure 8, asymmetries between positive and negative τ_o occur because the wedge must be centered in front of the observer. In addition, wedge LOS widths considered in the bottom panel are enough to shift the black line at large ϵ from its symmetric asymptotic value of 45° even for negative τ_o solutions, since the wedges are “cropped” as they extend past the observer at $+215r_\odot$.

$\frac{w}{2d} \ll 1$ will have essentially zero error τ_{diff} (not considering other sources of error, e.g. measurement error (DeForest, Howard, and Tappin, 2013b)), except at the TS and then to a degree quantifiable by Equation 52. Larger values of $\frac{w}{2d}$ ultimately result in the asymptotic solution $\tau_{pol} = 45^\circ$, as seen in the position of the black lines on the left hand side of the bottom panel of Figure 9.

Observations indicate that structures expand as they move outward, leading to increasing LOS width with increasing ϵ . In Figure 10, we assume that our wedge is an intersection with a sphere of diameter w , which expands self-

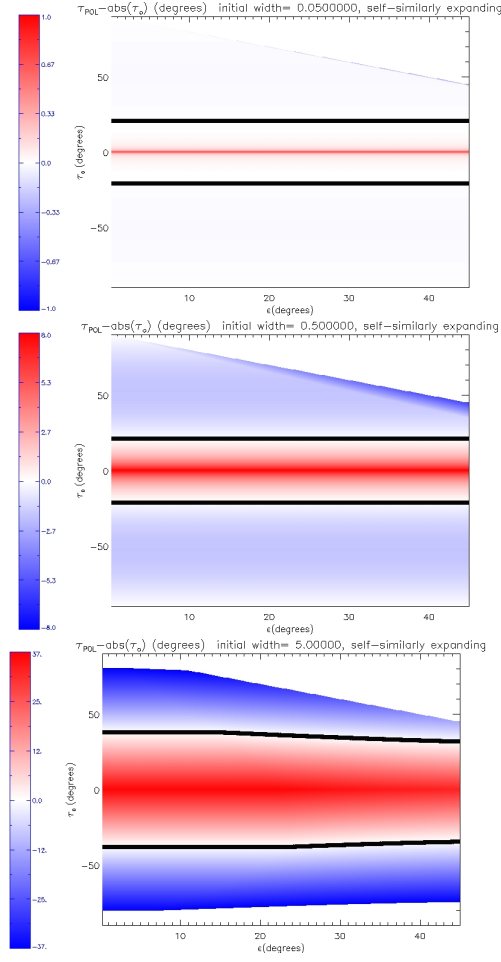


Figure 10. As in Figure 8 but with the LOS width changing as expected for a self-similarly expanding wedge with initial LOS widths $w_{ss} = 0.05, 0.5, 5.0r_{\odot}$ at initial height $r_{ss} = 1r_{\odot}$.

similarly² as it moves outward, i.e.,

$$w(r) = \frac{w_{ss}}{r_{ss}} \cdot r \quad (53)$$

²We recognize that a self-similar expansion is an oversimplification for CMEs, with in-situ statistical evidence for overall expansion at a rate less than self-similar (Bothmer and Schwenn, 1998; Gulisano et al., 2010; Zhuang et al., 2023) and variation observed with heliospheric distance (Lugaz et al., 2020; Zhuang et al., 2023), which would result in increased localization with heliocentric distance. This could particularly significant for embedded structures such as a prominence, which has been observed to expand much more slowly than the rest of the CME (Zhuang et al., 2025).

where w_{ss} and r_{ss} are constants of the self-similar expansion. Then, since

$$r = \frac{d}{\cos(\tau_o)} \quad (54)$$

we see that

$$\frac{w}{2d} = \frac{w_{ss} \cdot \cos(\tau_o)}{2r_{ss}} \quad (55)$$

Thus the self-similar expanding solution behaves almost like the $\frac{w}{2d}$ solutions of Figure 9, subject to a $\frac{\cos(\tau_o)}{2}$ scaling, and a self-similarly expanding structure of initial linear width $w = 0.05r_\odot$, $d = 1.0r_\odot$ will remain localized throughout its self-similar expansion. As in Figure 9, the middle panel represents a case where the wedge has become too large for localization, and the bottom panel a case that is nearing the infinite LOS width limit where $\tau_{pol} \rightarrow 45^\circ$, regardless of wedge center position τ_o . In this case, the wedge has initial LOS width $w = 5r_\odot$ at $d = 1.0r_\odot$ (such as that studied in Bemporad and Pagano (2015)) and so white light polarization data is not a good diagnostic of center position along lines of sight that intersect it over such an extended distance.

In summary: the degree of localization of a structure depends not just on the linear LOS width w of the structure being observed but also on the elongation angle ε , as represented by the dimensionless parameter $\frac{w}{2d}$. A self-similarly expanding structure will essentially maintain this critical parameter along its radial trajectory, so in such cases, knowledge of the structure's width at its origin can establish the degree to which white-light polarization data can diagnose the structure's 3D location throughout its trajectory. If it is in the localized, e.g. $\frac{w}{d} \cos^2(\tau_o) \ll 1$ regime, the error (which is maximum at the TS) can be quantified by Equation 50.

3. Polarization Diagnostics of CMEs

We now use a 3D model of a CME (Section 3.1) to show how polarization images and movies can remove the front/back ambiguity of CMEs and address ambiguities in trajectory/size (Section 3.2). We also use the model to demonstrate how locating the 3D position of CME substructures might be used to establish chirality, or direction of twist, within a CME (Section 3.3).

3.1. Twisted Croissant Model

Analytic models are useful for building insight and testing our diagnostics. We employ a croissant type CME model — essentially a hollow shell of density with a twist (Figure 11) The geometry of our model is similar to the graduated cylindrical shell (GCS) model (Thernisien, Howard, and Vourlidas, 2006; Thernisien, Vourlidas, and Howard, 2009), but is created with a different approach which offers the potential to easily create more complex shapes. For example, an overall twist can be applied to the croissant model. The model is initialized by defining the location of the inner tube axis, and parameters such as the twist, orientation,

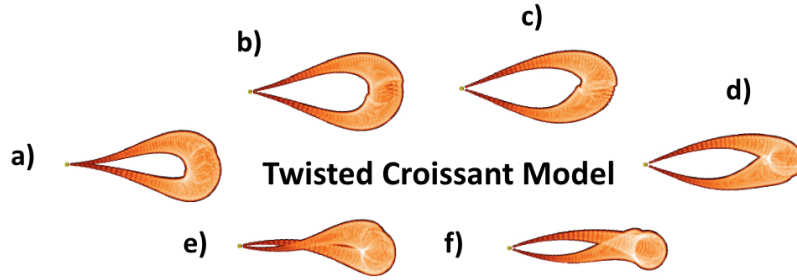


Figure 11. pB synthesized twisted croissant model, shown here rotating about the direction of its trajectory to illustrate its 3D structure. [MOVIE](#)

or leg separation are applied to this inner axis. The location of the tube sheath is then calculated in relation to the inner axis by defining the radial distance (or flux tube width), which expands from the CME footpoints to the apex. See Appendix B for further details.

This model has been incorporated into the FORWARD SolarSoft IDL modeling framework (Gibson et al., 2016), allowing forward modeling along lines of sight to form 2D projected images of, e.g., pB , tB , PR , τ_{pol} , x_{pol} , and the ground truth τ_{COM} and x_{COM} .

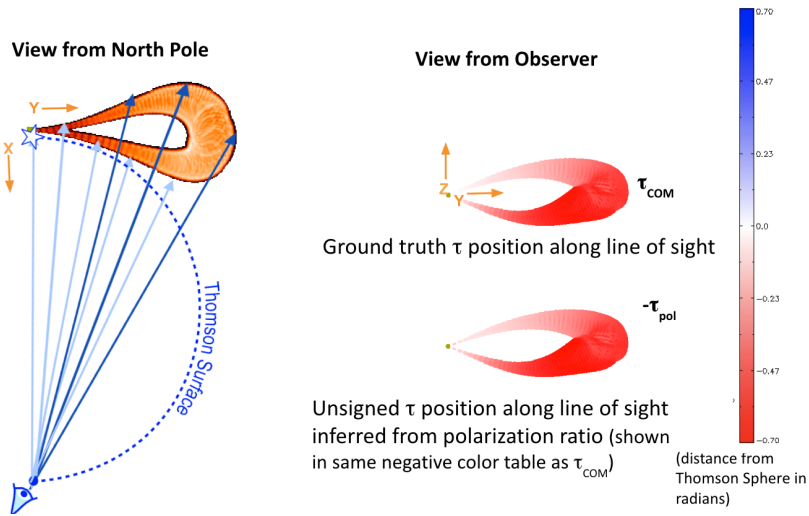


Figure 12. Polarization reveals distance from Thomson Sphere (TS). (left) The CME (twisted croissant model) as in Figure 11 erupting from the West limb, as viewed from the North pole. The lines of sight are shaded in progressively darker shades of blue to illustrate distance from the TS of the points of intersection with the croissant. (right top) τ_{COM} ground-truth calculated center of mass along the line of sight from the observer (eye shown in left image), and (right bottom) τ_{pol} calculated from forward-modeled synthetic pB and tB . The latter is unsigned, and the negative choice here is appropriate for all points along the edge of the CME as it lies completely behind the TS.

Figure 11 shows synthesized pB for a model CME erupting at the solar West limb. The images $a - f$ show how the line-of-sight-integrated pB changes if the twisted croissant rotates about the Y -axis. Figure 12 shows that the τ_{pol} calculated from forward-modeled pB and tB reproduces the (unsigned) distance from the TS, τ_{COM} . Note that the lines of sight shown in the left side of the figure each only intersect one point at the edge of the twisted croissant, because the edge that is positive x is also positive z (i.e., above the heliographic equator), while the edge that appears behind the X -axis from the North pole view of the left-hand side is below the heliographic equator (negative z) as viewed from the Earth and as shown in the images on the right-hand side. Such tangent lines of sight are intrinsically localized as discussed in Section 2.5.

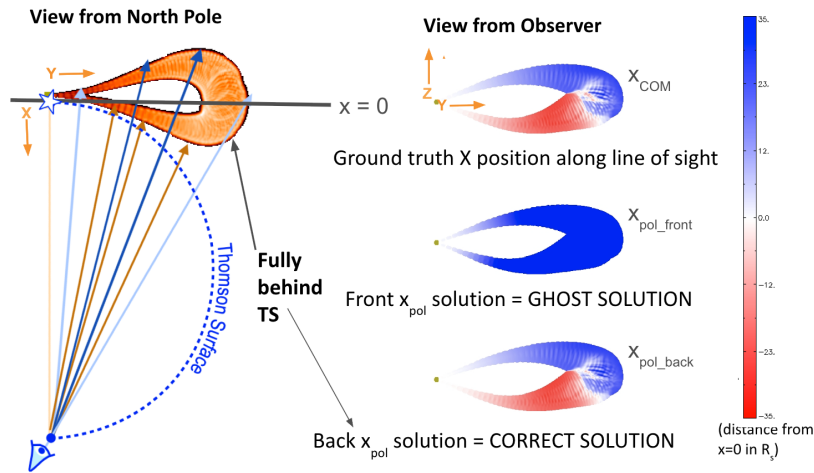


Figure 13. Polarization reveals distance from $X = 0$ plane (x_{pol}). (Left) The twisted croissant CME model as in Figure 12. The lines of sight here are shaded blue/red to indicate the croissant’s edge distance (negative/positive) from $x = 0$. (right) x_{COM} from the observer (eye shown in left image) and x_{pol} calculated from forward-modeled synthetic pB and tB . The latter has two solutions as discussed in the text (Equation 22) and shown in the middle and bottom images. The choice corresponding to negative τ_{pol} (bottom) is appropriate for this CME as it lies completely behind the TS.

In order to specify the position of the croissant edge in three dimensions, it is useful to calculate it in terms of distance from the $x = 0$ plane, i.e., x_{pol} . This then can be combined with a projection of the image onto the Observing Plane of Sky (YZ ; see Figure 1) along with knowledge of how the observers lines of sight intersect said plane, in order to yield $X - Y - Z$ coordinates of the edge (Equations 22-24). Equation 22 has two solutions for x_{pol} corresponding to the τ_{pol} in front of/behind the TS — we will refer to these as the “front” and “back” solutions. In the case shown in Figure 13, the CME lies entirely behind the TS and so the x_{pol} corresponding to the back solution is the correct one, while the x_{pol} corresponding to the front solution is the so-called “ghost” solution (DeForest, Howard, and Tappin, 2013b), which we now discuss.

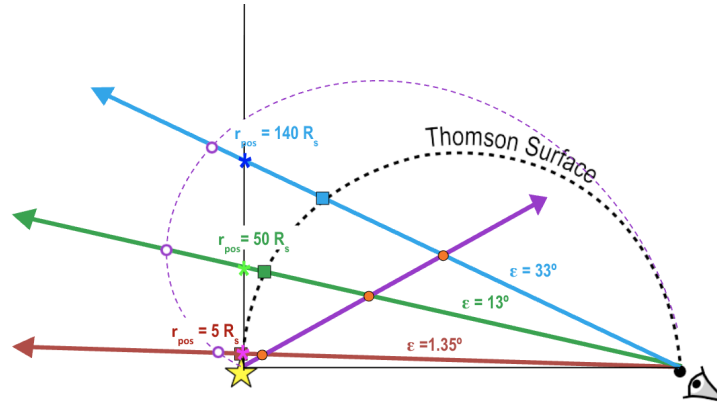


Figure 14. Two distinct trajectories arise from time series of polarization data. The solid purple line shows the true trajectory of a CME leading edge as it moves toward the observer, while the dashed purple curve shows a “ghost” trajectory as described in the text. The red, green and blue lines of sight intersect the TS at the positions indicated by colored squares, and the $x = 0$ plane as indicated by the colored *. The distance from the TS determined from PR , i.e., τ_{pol} , is indicated by orange dots in front of the TS (front solution), and purple circles behind the TS (back solution). Figure adapted from DeForest, Howard, and Tappin (2013b).

3.2. Tracking CME Trajectories

DeForest, Howard, and Tappin (2013b) explored the front/back of TS ambiguity implicit to analyzing white-light polarization data and demonstrated that the ambiguity can be removed for moving structures in wide-field heliographic images. We briefly review this now, and show how both movies and single images of CME x_{pol} might be used to establish whether a CME is approaching or receding from the observer at Earth.

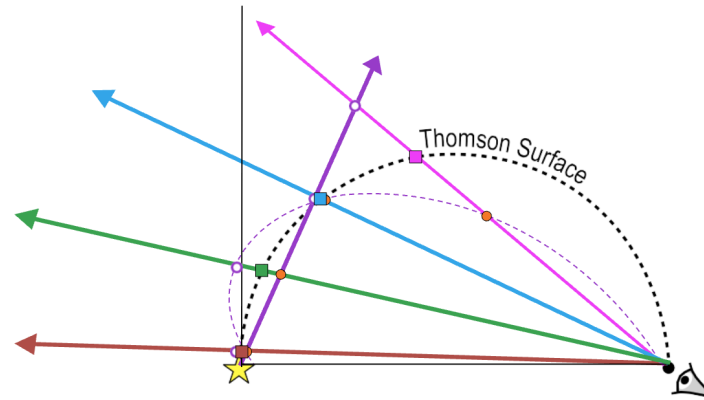


Figure 15. Approaching CME front as in Figure 14 but with a higher inclination trajectory that crosses the TS closer to the Sun. Note that the first two points along the true trajectory (solid purple line) are solid orange dots (positive τ_{pol} or front solutions), while the next two points are purple circles (negative τ_{pol} or back solutions), and the converse is true for the ghost solution (dashed purple line). Figure adapted from DeForest, Howard, and Tappin (2013b).

3.2.1. Revealing the ghost trajectory

As we have discussed above, the more compact a structure is, the more straightforward it is to locate its position in 3D. An important case is that of the CME leading edge, which by definition has a tangent (compact) intersection with any given line of sight as discussed above (Howard et al., 2013). This is generally true for any surface, not just spherical ones, as it is a consequence of the interior-extremum theorem of calculus. Note that, for most CMEs, the 2D “leading edge” is slightly different than the 3D front propagation location (“nose”) of the CME, an effect that leads to at least some uncertainty in CME direction and propagation speed, even if the CME nose location is fully known. See Malanushenko et al. (2025) for further discussion.

For coronagraphic images, there is a front-back ambiguity inherent to Equation 22 that is unavoidable, because the TS is nearly aligned with the $x = 0$ plane, and thus the two solutions are essentially symmetric about this observing plane of sky. Because heliospheric imagers have a wide field of view, however, the curvature of the TS breaks the symmetry, so that a time series of x_{pol} for an Earth-approaching CME produces a radial “true” trajectory, and a curved “ghost” trajectory as shown in Figure 14. From this it can be seen that the front solution (orange dots) follow the correct trajectory with monotonically increasing radial distance and always positive x_{pol} , while the back solution (purple circles) trace out the ghost trajectory that first recedes and then advances toward the observer. In this case, all points of the true trajectory lie in front of the TS (positive τ_{pos} — orange dots), while all the points shown on the ghost trajectory are behind the TS (negative τ_{pos} — purple circles).

Figure 15 shows a steeper trajectory that crosses the TS closer to the Sun. In this case, the true trajectory includes some points from the front solution and some from the back, as does the ghost trajectory. Nevertheless, the true solution can be found by making the choice for each time step of the trajectory closest to radial. See Malanushenko et al. (2025) for a demonstration using simulated PUNCH data synthesized from a global MHD model.

The solutions for an Earth-receding CME are qualitatively different than the Earth-advancing CMEs shown in Figures 14 and 15. Figure 16 shows that the true trajectory of a receding CME leading edge is radial and always negative x_{pol} , while the ghost trajectory is nonradial and always positive x_{pol} . The former is made up of τ_{pol} solutions behind the TS, and the latter of solutions in front of the TS.

In summary: if the two (front/back of TS) solutions for position x_{pol} for the CME leading edge are both positive at any point in the CME’s passage, the CME must be Earth-approaching. If one is positive and one negative, it is generally necessary to follow the time series of the radial position of the front and back solutions (calculated via Equations 22-24) in order to establish a radial trajectory made up of some combination of front and back solutions; the sign of x in that trajectory then determines whether the CME is Earth-approaching or Earth-receding.

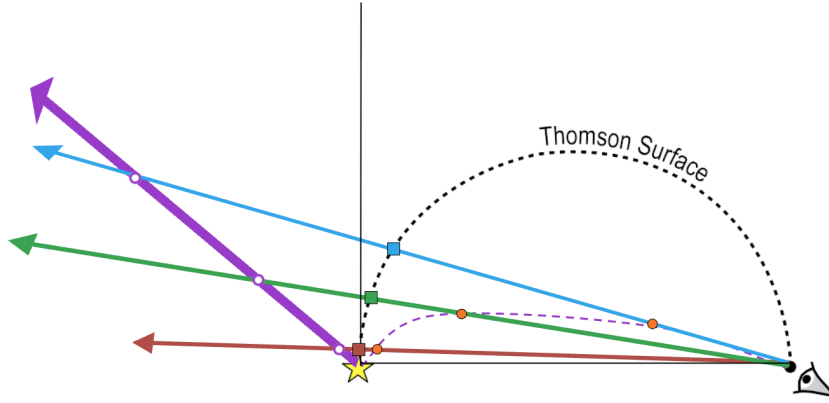


Figure 16. CME moving away from observer. The solid purple line shows the true trajectory of the CME leading edge, and the dashed purple line shows the ghost trajectory.

3.2.2. Imaging halo CMEs

As described above, and discussed in DeForest, Howard, and Tappin (2013b), disambiguation for a CME leading edge is possible with a time series by plotting the radial position vs time of the front and back solutions for the leading edge (Laurent, 2025). But CMEs are more than a single leading edge, and information about their location is encoded in the polarization data from their full extent. This has been demonstrated by Jarolim (2025), who used a physics-informed-neural-network approach to track CME trajectory from synthetic images of eruptions. In this section, we consider in general how images and movies of CME x_{pol} might be used to establish whether a CME is advancing toward or receding from the observer.

Figure 17 shows images for a Earth-approaching case similar to Figure 14. On the left, the view from the North pole shows images of pB for the CME for three time steps as the flux rope expands self-similarly. The arrows connect the observer to points tangent to the flux rope (orange circles) and extend toward the plane of the sky with dashed lines, ending in the purple circles that indicate the ghost position on the other side of the TS. The view from the observer is shown on the right side, with the ground truth X_{COM} showing the true location of the flux-rope edge in front of the $x = 0$ plane (red), captured also in $x_{pol_{front}}$.

The ghost solution $x_{pol_{back}}$ is by definition always behind the TS , but the most expanded stage has leading-edge ghost positions in front of the $x = 0$ plane, yielding a multicolored image (bottom right of Figure 17). This can only happen for an Earth-approaching halo CME. As Figure 18 shows, a halo CME receding from the observer will maintain opposite colors for $x_{pol_{front}}$ and $x_{pol_{back}}$, and will asymptotically approach an unchanging apparent size.

Figure 19 introduces another use for polarization, the disambiguation of situations where non-parallel lines of sight lead to a similar appearance for narrow, fast CMEs vs. wide, slow CMEs. The two cases shown correspond to wide and narrow halo CMEs (also shown from a North Pole view in Figure 20), and illustrate how polarization data yield very different results despite similarity in

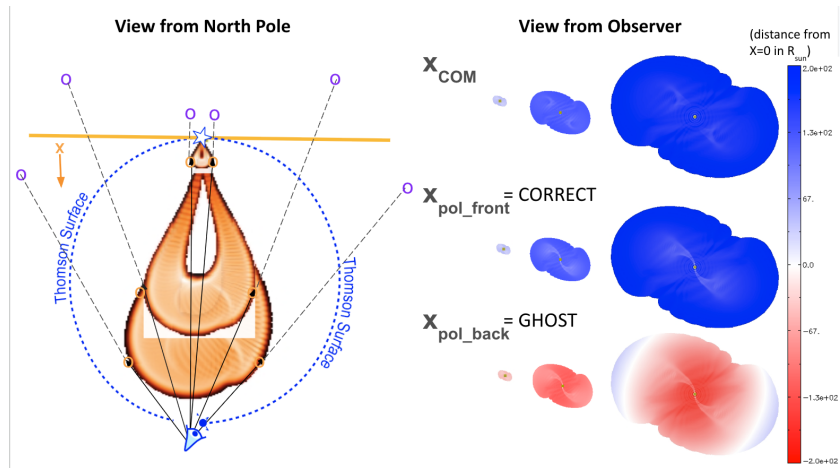


Figure 17. Halo CME advancing toward the observer. Left: view from the North pole of the CME in pB for three time steps. Orange circles show where lines of sight intersect the flux rope edge in the x_{pol_front} solution, purple circles show the ghost x_{pol_back} solution. Right: View from the observer for the three time steps for ground truth x_{COM} (top), the correct, positive- x solution (middle), and the ghost primarily negative- x solution (bottom). The fact that parts of the most expanded CME shows both signs in x_{pol_back} is a smoking-gun signature of an Earth-approaching halo CME.

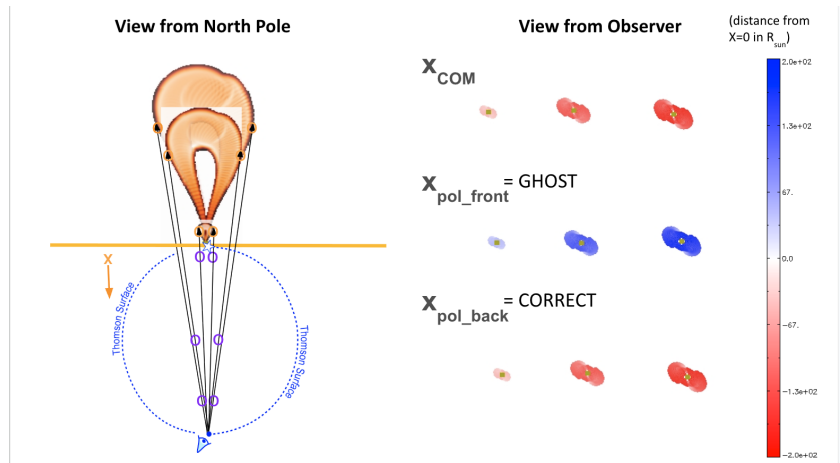


Figure 18. Halo CME receding from the observer. As in Figure 17, but with x_{pol_back} being the correct solution and x_{pol_front} the ghost solution. Note that the solutions asymptote to a maximum apparent size as lines of sight become effectively parallel.

pB projected size and shape. The time series of these polarization images can be used to establish the leading edge trajectory as described above, establishing CME speed and predicting time of arrival. But even a single image is enough to show that the wide CME is much closer to $x = 0$ than the narrow CME, and thus moving more slowly.

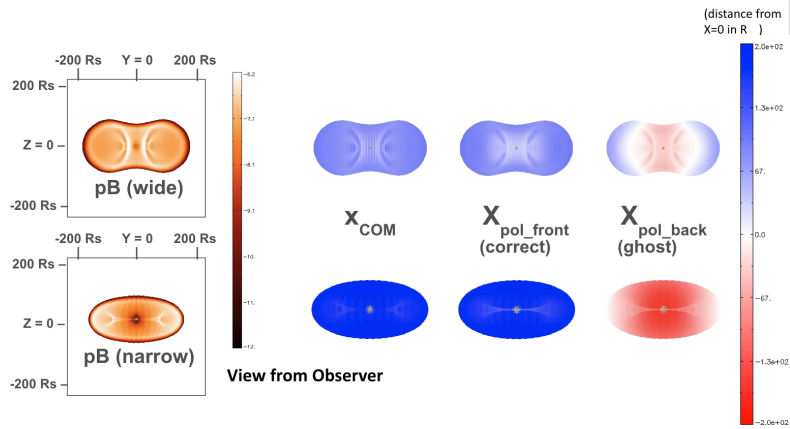


Figure 19. Wide vs narrow halo CME approaching the observer. Left column shows wide (top) and narrow (bottom) halo CMEs (see Figure 20) from the observer's point of view. Right three columns show that despite the fact they have the same projected apparent size and aspect ratio, the polarization ratio yields very different results and immediately shows the wide CME (top row) is farther from the observer, as evidenced by the lower distance from $x = 0$ (paler red/blue in images).

We note that Figures 17-20 represent cases where lines of sight intersect multiple structures, in particular, as Figure 20 demonstrates explicitly, all but the leading edge (tangent) lines of sight intersect both sides of the croissant. Nevertheless, Figure 19 shows that x_{pol_front} reproduces x_{COM} for most points in both projected CMEs. See de Koning et al. (2025) for further demonstration of

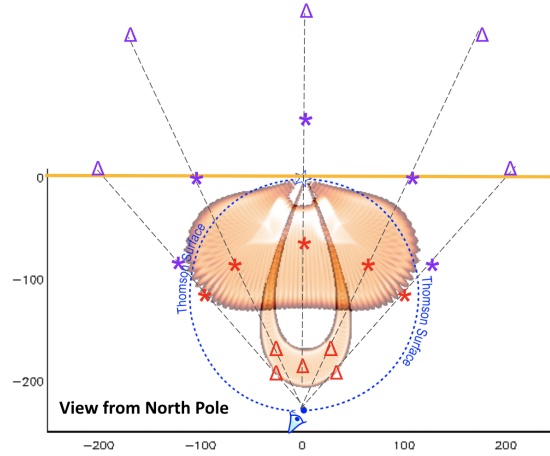


Figure 20. Wide vs narrow halo CMEs can be disambiguated by polarization. Red triangles show the correct x_{pol_front} solution for the various lines of sight through the narrow CME, while purple triangles show the ghost x_{pol_back} solutions on the opposite side of the TS. Similarly, red asterisks show the correct x_{pol_front} solutions for the wide CME, while purple asterisks show the ghost x_{pol_back} solutions. In this case, only the leading edges for each CME can be thought of as superparticles and located by x_{pol_front} , while the other lines of sight intersect multiple structures and result in a representation of center of mass equivalent to x_{COM} .

the resiliency of the superparticle approximation to the superposition of multiple structures along the line of sight.)

In summary: even a single snapshot of a halo CME can yield information about whether it is Earth-approaching or Earth-receding. It can also provide immediate information about whether it is wide and slow vs narrow and fast.

3.3. Polarization Diagnostics of CME Substructures

CMEs are generally expected to incorporate coherently-twisted magnetic fields, i.e., magnetic flux ropes. The chirality, or handedness of magnetic twist of the flux rope is significant, because they provide information about the direction of the magnetic fields that may interact with the Earth's magnetic field (Cane, Richardson, and St. Cyr, 2000; Yurchyshyn, Wang, and Abramenko, 2003; De-Forest, de Koning, and Elliott, 2017b; Pal, 2022) Figure 21 illustrates this for two examples of right- and left-handed flux ropes expanding out from the Sun.

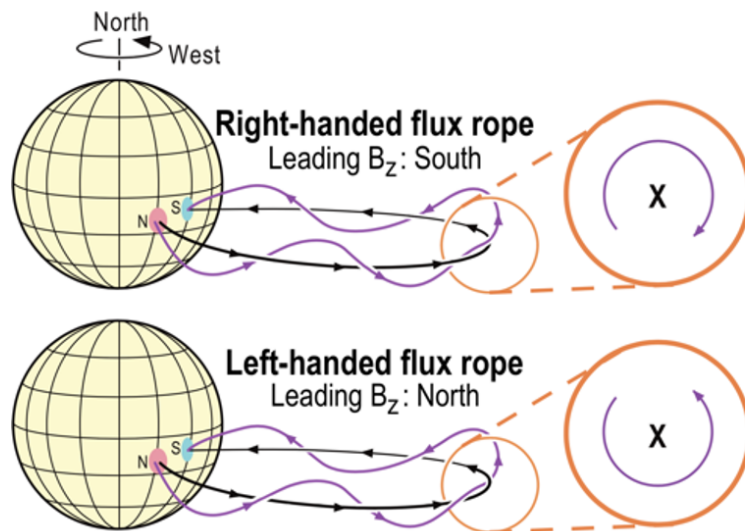


Figure 21. Representation of two flux ropes, right-handed and left-handed, with the same polarity footpoints at the Sun. As they expand into interplanetary space, we see the right-handed flux rope has South B_z at its front, while the left-handed flux rope has North B_z at its front.

3.3.1. Diagnosing chirality

By establishing the location of helical CME substructures using polarization, it is possible to establish chirality from the direction the structure curves when traced from front to back. If clockwise, it is right-handed, while if counterclockwise, it is left-handed (see Figure 22). The ability to do this was demonstrated using

coronagraph observations in DeForest, de Koning, and Elliott (2017b), where white light polarization data was used to establish the distance from the $x = 0$ plane for a substructure within the erupting CME. Since the CME was observed from two vantage points (SOHO and STEREO), the front vs back solution was easily disambiguated. The x position of the substructure was then traced from front to back along a C-shaped curve, establishing a clockwise direction, and thus right-hand twist. This particular CME was later observed as a magnetic cloud, which also showed right-handed twist, consistent with the determination made from the coronal polarization data.

To demonstrate this, Figure 23 forward models a simulation of an erupting magnetic flux rope close to the Sun (Fan, 2018). This MHD model incorporates simple empirical coronal heating, optically thin radiative cooling, and field-aligned thermal conduction, and thus allows the formation of prominence condensations, which we will locate using polarization data. For three sample time steps, we first calculated the density center of mass (x_{COM} ; middle column) and then forward modeled synthetic pB and tB and calculated x_{pol} (right column). Note that thresholding has been employed to isolate the substructure from the background. In particular, only densities greater than the threshold values indicated in the figure caption are used in the center-of-mass calculation. For the polarization calculation, we have subtracted an earlier timestep (at $t = 36.17$

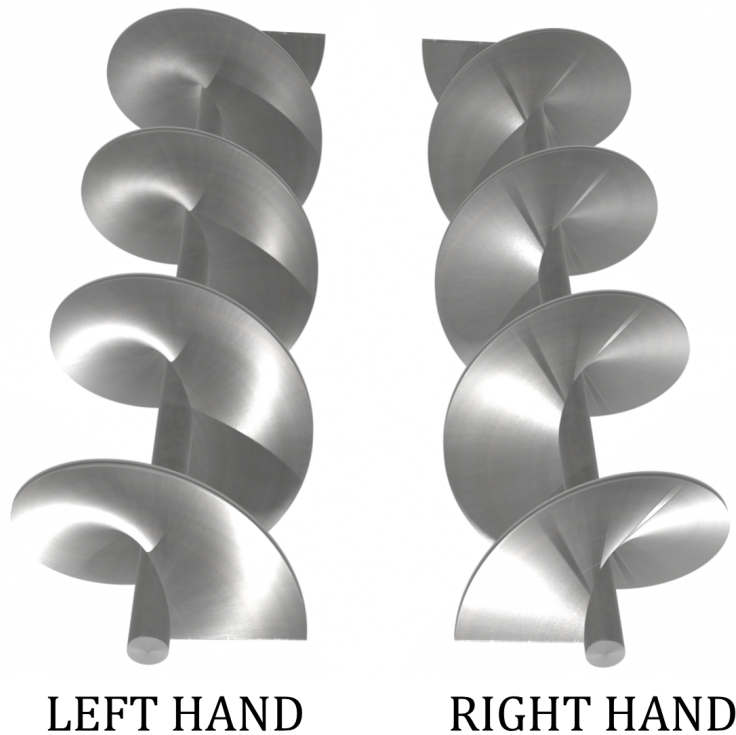


Figure 22. Chirality can be determined by considering the direction a structure curves when moving from front to back, clockwise (right-handed) or counterclockwise (left-handed).

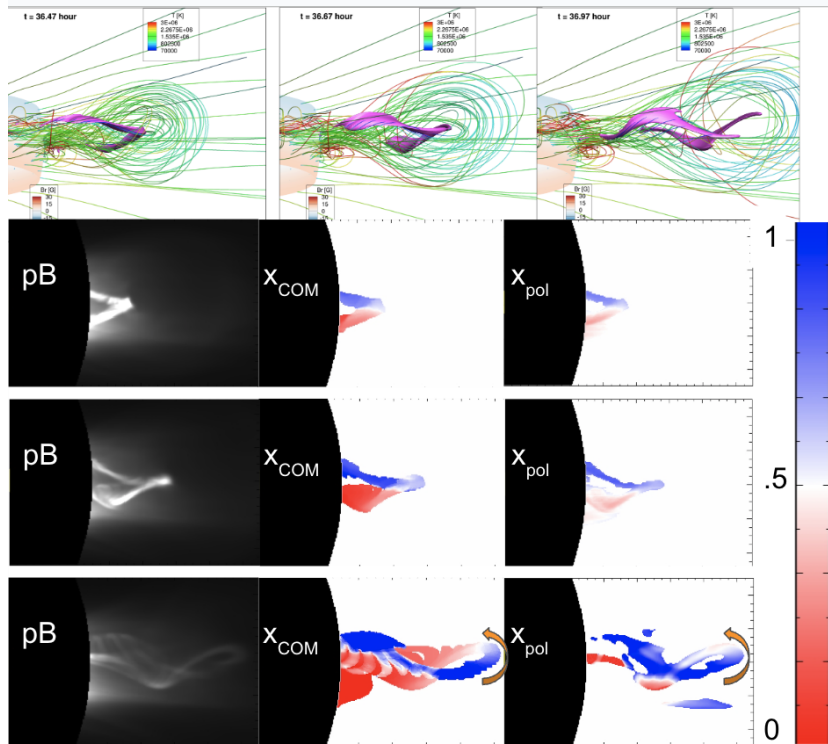


Figure 23. Locating the structure of an erupting prominence/filament based on forward modeling of the Fan (2018) model of an erupting prominence-carrying flux rope. Top row: magnetic field lines of the erupting flux rope and the associated prominence material outlined by the purple isosurface of temperature (at $T = 80,000$ K) at three successive time instances indicated in the images. Next three rows: Left column shows the corresponding forward modeled white light pB , where the dense prominence material carried by the erupting flux rope is clearly seen as the bright core of the CME. Middle column shows the position along the line of sight of the density center of mass (x_{COM}), thresholded $n_e > 10^8, 10^8, 5 \times 10^7 \text{ cm}^{-3}$ for the three time instances, and the right column shows the position extracted from background-subtracted synthetic polarization data as described in the text, with thresholded $pB > 12, 9, 0.6 \times 10^{-8} B_{\odot}$ for the three time instances. Distance from the $x = 0$ plane of sky is indicated by color, in solar radii, offset so that the change from red to blue occurs at the center of the flux rope, $x = 0.5$. The arrow in the bottom row traces the direction the filament curves at the apex: counterclockwise from front to back, and thus left-handed chirality, which is consistent with the writhing of the (purple) filament shown in the top row. Occulting disk is set at $1.5r_{\odot}$.

hour) and then have run the calculation using only pixels with pB greater than a thresholded value (indicated in the figure caption).

The x_{pol} we have used is the front solution, as we have centered the flux rope 20 degrees in front of the $x = 0$ plane so that it lies entirely in front of the TS, and assume that this has been established by, e.g., EUV observations projected against the solar disk. In addition, the rope is rotated 10 degrees clockwise around the Y axis. The position along the X-axis is indicated by the color bar: note that unlike previous figures, the color bar is not centered on $x = 0$ but rather the center of the rope, in order to make it easier to see the direction of twist.

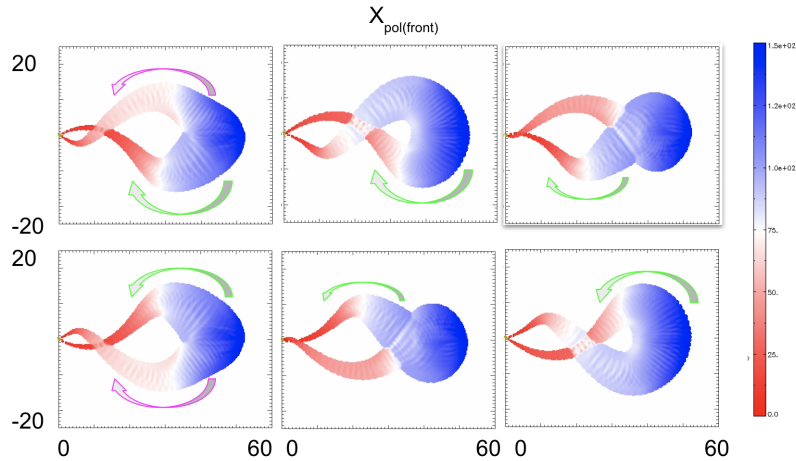


Figure 24. Twisted croissant CME model for right-handed (top) and left-handed (bottom) flux ropes, for three orientations of the ropes (rotating about the Y -axis. Axes are plotted in units of R_{\odot} , and color bar shows x_{pol} in the same units. The green curved arrows show circulation about an axis that establishes flux rope chirality, while the pink arrow tracks a misleading apparent circulation of the opposite sign (see text). **MOVIE.**

The first thing to note is the general agreement of x_{COM} and x_{pol} . This substructure is localized, but some small difference is expected due to the error associated with proximity to the TS, and indeed we see as expected $x_{pol} > x_{COM}$ near $x = 0$, manifesting as red \rightarrow pink. Circulation about the flux rope axis is harder to determine, especially for the first two time steps. However, by the third time step, the rope has expanded out far enough to indicate a counterclockwise rotation when measured front to back (blue to red). An analysis of the rotation of the simulated flux rope (counter-clockwise when viewed from above) provides further, complementary evidence for left-handed twist (Green et al., 2007; Demoulin, 2007; Gibson and Fan, 2008).

Polarization analysis of erupting structures such as the prominence modeled here may be done in the low-to-middle corona using the pB and tB data from ESA’s Proba-3 ASPIICS mission (Zhukov et al., 2025). In this region, the TS lies along the $x = 0$ plane and does not have the symmetry-breaking curvature found in a wider field of view. The front-back ambiguity is thus harder to disentangle (see, e.g. Dai et al. (2014)). One way around this is to use multiple viewpoints, e.g., polarization data from the STEREO spacecraft (Dai, Wang, and Inhester, 2020). Another way is to monitor an eruption starting in the ASPIICS field of view as it continues into the PUNCH field of view, and use the polarization data from PUNCH to help disambiguate the polarization information in the lower, ASPIICS field of view.

To simulate twist in the outer, PUNCH field of view, we turn to our twisted croissant model. Figure 24 plots a somewhat more twisted model than Figure 11. Again, we have positioned this structure so that it lies entirely $x > 0$, and make the assumption that this has been established by following the CME trajectory

as described above. Also again, we have centered the color table on the center of the rope, rather than on $x = 0$.

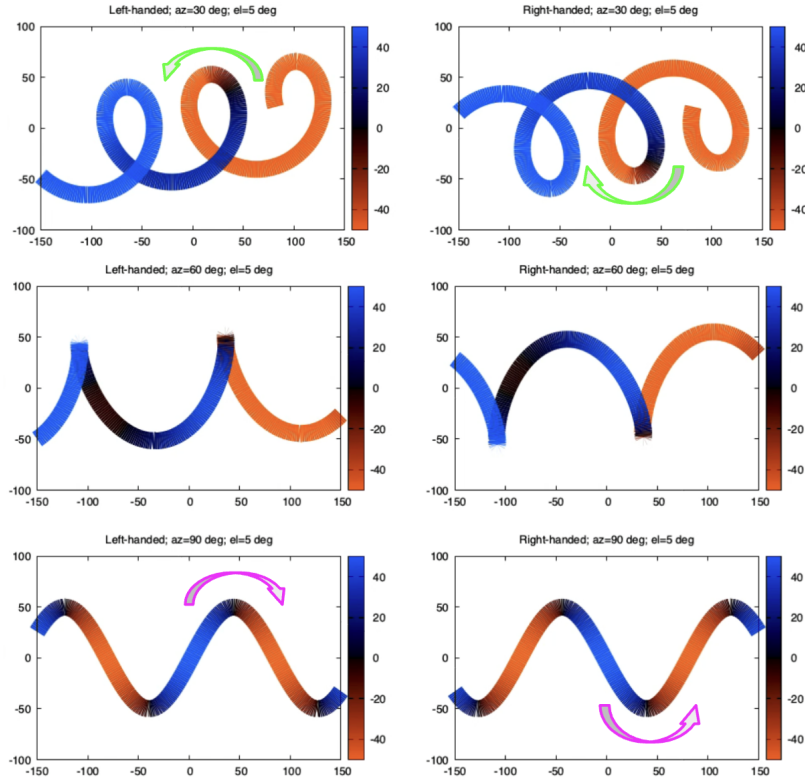


Figure 25. Simple helical model with blue-red color table indicating distance in the foreground (blue) and background (red). Left (right) column is left(right)-handed rope. Orientation of the rope is rotated clockwise about the vertical axis. The green curved arrows show circulation about an axis that establishes flux rope chirality, while the pink arrow tracks a misleading apparent circulation of the opposite sign (see text). [MOVIE](#)

The x position of the center of mass is well captured from synthetic polarization data as described above, and the positive chirality can generally be determined by following curves from front to back (blue to red), as shown by the green curved arrows. However, the pink curved arrow shows a potential ambiguity for the first orientation of the rope, which appears to rotate counterclockwise front-to-back in its northern portion as opposed to the clockwise rotation seen in its southern portion throughout (and vice versa for the left-handed rope in the bottom row).

To shed light on why this occurs, we present an even more idealized model in Figure 25. As in Figure 24, for some orientations the axis of rotation is clear, and the circulation about it correctly indicates the sign of chirality. However, the bottom panel shows a view perpendicular to the axis where following a curve from front to back yields the wrong sign.

In order to remove this discrepancy, it is necessary to not rely on any one projection, but rather to use the full 3D location of the substructure (Equations 22-24) to establish circulation about an axis.

In summary: To locate the position of a CME substructure in 3D, it is first necessary to examine the CME trajectory to eliminate the ghost solution. After this, its 4D space-time trajectory may be obtained and potentially used to diagnose chirality.

4. Discussion and Conclusions

In this paper, we have demonstrated how the polarization ratio PR contains useful information about the two limits discussed in this paper, i.e., that of a superparticle, or compact mass along the line of sight, and that of spherically symmetric density distribution. The former is dependent on the degree to which the mass is localized, which we have shown has a non-trivial dependence on linear LOS half-width and line-of-sight viewing angle as characterized by the critical width parameter, $\frac{w}{2d}$. The latter represents a local diagnostic of the global density radial falloff that might be used to study variations in the background solar wind as a function of time – for example global responses to large CMEs, or solar cycle timescale variation.

We have used forward models of CMEs to illustrate how the 3d location of the edges of CMEs can be determined and have demonstrated that even with multiple compact masses along a line of sight, the COM density position can be reproduced. We have shown how individual polarization images can establish whether a CME is approaching or receding, and whether it is wide and slow vs narrow and fast. We have demonstrated that while flux rope chirality (or handedness) can be deduced by tracing the curvature of CME substructures, it requires consideration of all projections of the 3D surface mapped out by polarization.

The models used in this paper are idealized, as our goal has been to establish proof-of-concept for the methods described and to deepen our understanding of the sources of uncertainty for polarization diagnostics. We refer the reader to Malanushenko et al. (2025) for an application of these diagnostics to white-light CME data synthesized from more sophisticated global MHD simulations. Of course, real data introduces a range of additional practical difficulties. In particular, imaging data from PUNCH and elsewhere are subject to noise. As described in Section 3.2 of (DeForest et al., 2025), PUNCH has been designed with sensitivity requirements intended to allow 3D tracking of features of expected brightness. There is also the problem of disentangling background structures from CMEs, which time-differencing as employed in Figure 23 cannot fully address. However, we note sophisticated means exist for isolating CME signal from the background without amplifying noise (Morgan, Byrne, and Habbal, 2012), and these have been applied successfully to real time operations (see, e.g., https://solarphysics.aber.ac.uk/Archives/cme_realtime/realtime_catalogue.html).

Setting aside noise, we have demonstrated some intrinsic error sources associated with polarization feature localization, which can be quantified if we are in

the small-width limit. Just as importantly, we have explored and demonstrated the limits of the superparticle approximation for polarized 3D analysis, including where and how the small-width limit breaks down so that there potential for the information from the polarization to be misinterpreted. As the critical width parameter $\frac{w}{2d}$ transitions toward the infinite width regime, τ_{pol} loses information about the wedge center position τ_o , and the apparent over- and under-estimate in $\tau_{diff} = \tau_{pol} - |\tau_o|$ no longer represents an error on position localization, but simply the difference between any given τ_o and the value of τ_{pol} that happens to characterize that $\frac{w}{2d}$. For this reason, the exact solutions, $\tau_{diff} = 0$ (black lines in Figures 8-10), are essentially meaningless and potentially misleading: A broken clock is accurate twice a day.

It is important to emphasize that even such extended features, if visible in an image plane, can be localized along the lines of sight near their image-plane edges. As we have discussed, we can safely assume that CME “leading edges” are localized at a point of tangency between the line of sight and the CME envelope, and the superparticle approximation therefore applies. For CME substructure or mesoscale “blobs” in the solar wind, one should establish $\frac{w}{2d}$, or, analogously, the near-Sun width for a self-similarly expanding feature, in order to establish how localized a feature is and to what degree the superparticle approximation may be used to characterize its structure overall. We note that features that expand at a less than a self-similar rate can actually become more localized as they travel outward, e.g., the compact prominence tracked by Zhuang et al. (2025).

SIRs are an intermediate case in that they have global scale but form comparatively thin manifolds and hence may be localized along some lines of sight where they are visible. Our assumption of a uniform density wedge is not generally appropriate for SIRs. de Koning et al. (2025) instead consider features of a given angular width Δ – equivalent to our $\frac{w}{2d} \cos^2(\tau_o)$ in the small-width limit and possessing the same definition of compactness under the assumption of uniform density (i.e., $2\Delta \ll 1$, equivalent to $\frac{w}{d} \cos^2(\tau_o) \ll 1$), but find a somewhat more stringent localization requirement when they assume a density profile of r^{-2} within their feature, i.e., $4\Delta \ll 1$. In between, they examine how PR might be combined with knowledge of either feature angular width or feature central angle to establish the missing variable.

There is thus clear benefit in supplementing polarization diagnostics with information about the size and structure of a feature being studied. Some promising approaches include geometric analyses of feature dimensions (Moraes Filho et al., 2024; López-Portela, Paz Miralles, and Lara, 2025), multiple viewpoints from different spacecraft and/or tomographic reconstructions (Morgan and Cook, 2020; Dai, Wang, and Inhester, 2020; Jackson et al., 2023; Jarolim, 2025), and global MHD simulations (Sachdeva et al., 2021; Lionello et al., 2023; Odstrcil, 2023; Pogorelov et al., 2024; Linan et al., 2025; Provornikova et al., 2025).

In final summary, white light polarization entrains important information about the structure and distribution of plasma in the young solar wind. By exploring the analytic limits of polarization analysis, we have determined practical limits of when and how polarization data may be used in the context of solar wind imaging – including with PUNCH.

5. Acknowledgments

PUNCH is a heliophysics mission to study the corona, solar wind, and space weather as an integrated system, and is part of NASA's Explorers program (Contract 80GSFC14C0014). S.E.G., Y. F., and A.M. acknowledge support of the National Center for Atmospheric Research, a major facility sponsored by the National Science Foundation under Cooperative Agreement No. 1852977. C. A. dK. acknowledges support from NASA grant N99055DS and AFOSR YIP program FA9550-21-1-0276, and C. A. dK., C. E. D., A. M., and S. E. G. acknowledge funding from AFOSR grant FA9550-21-1-0457. S. E. G. and C. E. D. acknowledge support from NASA grant 80NSSC21K1860 (US-coIs of the ASPIICS mission). E.P is supported by the AFOSR grant FA9550-21-1-0457 and AFOSR YIP program FA9550-21-1-0276.

Appendix A Definitions

See Figure 1 and DeForest et al. (2025) for illustration and further discussion of the quantities listed below. Bold-faced font indicates quantities known or directly measurable by PUNCH; regular font indicates derived quantities.

- Radial-Tangential Normal (RTN) coordinate system (Burlaga, 1984; Fränz and Harper, 2002).
 - **X axis** = Sun-observer line (positive/negative in front/behind Sun)
 - **Z axis** = projected solar rotation axis
 - **Y axis** = perpendicular to both X and Z in a right-handed system
- r_{obs} = distance between observer and Sun
- ε = elongation angle of line of sight (LOS) measured from X axis
- α = polar angle of intersection of LOS with Y-Z plane (Observing Plane of Sky), measured counterclockwise from Z axis about X axis.
- p = degree of polarization, $\frac{pB}{tB}$.
- r_{pos} = distance from Sun center to intersection of LOS with Y-Z plane
 - $r_{pos} = r_{obs} \tan \varepsilon$
 - With α , this specifies the location of the LOS-integrated observable on the Observing Plane of Sky
- d = distance of closest approach to Sun center of any LOS (impact factor; occurs at intersection of LOS and TS)
 - $d = r_{obs} \sin(\varepsilon)$
- PR = polarization ratio
 - $PR = \frac{1-p}{1+p}$
- χ = scattering angle
 - $\chi_{pol} = \pm \arccos(\sqrt{PR})$
- τ = angle along LOS; $\tau = 0$ is intersection of LOS with Thomson Sphere (TS), positive toward observer, negative away.
 - $\tau_{pol} = \pm \arcsin(\sqrt{PR})$
 - $\tau = \frac{\pi}{2} - \chi$
- ξ = out-of-sky-plane angle
 - $\xi(\tau) = \varepsilon + \tau$
- ψ = complement to ξ
 - $\psi(\tau) = 90 - \xi$
- r = distance to scattering point from center of sun
 - $r(\tau) = d / \cos(\tau)$
- s = distance from TS to scattering point for a given LOS (positive toward observer, negative away)
 - $s(\tau) = d \tan(\tau)$
- ℓ = distance from scattering point to observer (always positive)
 - $\ell(\tau) = r_{obs} \cos(\varepsilon) - s$

Appendix B Croissant Model

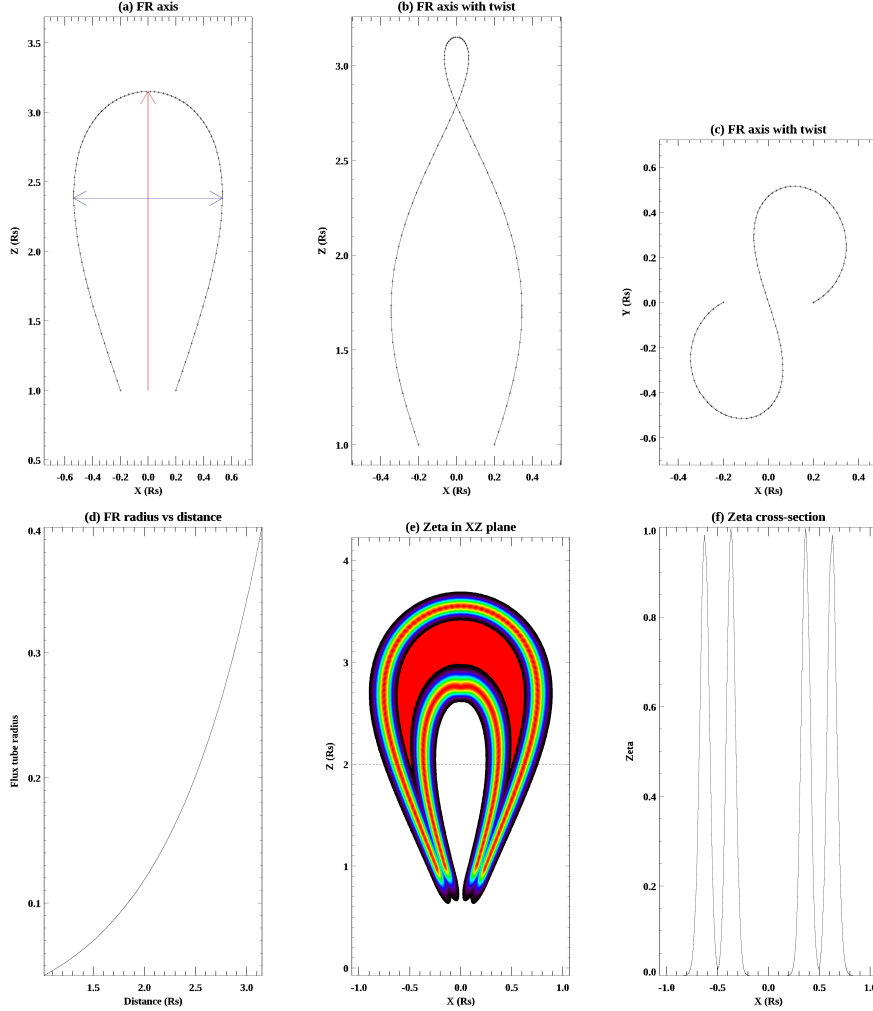


Figure 26. (a) The initial geometry of the CME flux rope central axis, as described by equation 56. The red arrow shows $r_{m,x}$, or the maximum distance at the axis apex. The blue arrows illustrate ΔX , set in this example to $\Delta X = 1$. (b) Example of applying a twist to the central axis, as viewed along the y axis and (c) along the z axis. (d) The flux rope radius w as a function of distance as given by equation 59. (e) ζ , or the normalized spatial weighting of density given by equation 60, defining the sheath around the central axis in the xz plane (for a non-twisted central axis). (f) ζ plotted along the dashed horizontal line in (e).

The model is initialized by defining the coordinates of a set of 100 points which give the location of an axis which lies along the center of the flux tube.

These are defined as

$$x = (r_{mx} - 1)\sin(t)\Delta X + tl/\pi \quad (56)$$

$$y = 0 \quad (57)$$

$$z = 1 + (r_{mx} - 1)\cos(t/2) \quad (58)$$

where t is a parameter with 100 points increasing linearly from $-\pi$ to π , r_{mx} is the maximum heliocentric distance (or apex) of the flux tube axis, ΔX is a parameter controlling the overall width of the flux tube (i.e. angular width separating the legs), and l is a parameter that controls how rapidly the legs expand with height to the defined overall width. In this initial configuration, the flux tube axis is embedded in the xz plane and is symmetric around $x = 0$ (or aligned with the north pole), as shown in Figure 26a. If required, a twist can easily be applied by a rotation around the z axis, with the rotation angle increasing from zero at $z = 1$ (minimum distance) to the maximum defined twist angle at $z = r_{mx}$, as shown in Figures 26b and c. An overall orientation can also be applied by rigid rotation around the z axis. A 3D rotation of the entire axis to the required central longitude and latitude relative to an observer, from its initial location centered on the z axis (or north pole), is then made.

The radius of the flux tube around the central axis is defined as

$$\rho = \rho_0 \exp([(r/r_{mx}) - 1]/h_\rho) \quad (59)$$

where ρ_0 is a parameter controlling the maximum radius of the flux tube (at the maximum or apex distance with default value 0.4 for $r_{mx} = 3.15$), r is the heliocentric distance of each point along the axis, and h_ρ is a parameter controlling how rapidly the flux tube expands with distance from the footpoints, with default value $h_\rho = 0.3$. ρ is shown as a function of distance in Figure 26d.

Once the geometry of the axis and the flux tube radii are defined the density distribution of the flux tube sheath is calculated. There are very efficient ways to do this computationally, but for compatibility with FORWARD calculations this is made on a full 3D grid of voxels defining the corona. The orientation of the local normal to the axis relative to solar x, y, z is calculated at each axis point. Looping through each point, indexed i , the coordinates of the voxels are translated to a new origin at that axis point, and the voxel coordinates rotated so that the yz plane is tangent to the curve of the axis at that point, giving a new set of coordinates for each voxel: x_n, y_n, z_n . A weighting at each voxel is defined as

$$\zeta = \exp(-[d_i - \rho_i]^2/\sigma_i - x_n^2/2\Delta s), \quad (60)$$

with $d_i = \sqrt{y_n^2 + z_n^2}$ and Δs the distance between each axis point. σ_i is a parameter controlling the thickness of the sheath, and is set by default to $0.0016r_i$ (so that the sheath thickness increases with distance). Looping through all hundred flux axis points, the maximum recorded ζ is retained at each voxel.

ζ is a spatial weighting ranging from zero to one: a two-dimensional cross-section is shown in Figure 26e, and a one-dimensional cross-section is plotted in Figure 26f. We set the total mass of the CME, and distribute that mass

appropriately by ζ . Furthermore, we apply a smooth function of height that distributes more of the mass at the CME apex compared to the footpoints. Without this function the CME legs dominate the brightness when FORWARD applies line-of-sight integrations. In principle, more realistic density distributions may be sought, although CME masses and density distributions are currently poorly constrained by observations.

References

- Altschuler, M.D., Perry, R.M.: 1972, On determining the electron density distribution of the solar corona from K-Coronameter data. *Solar Phys.* **23**, 410. DOI ADS.
- Baumbach, S.: 1938, Die Polarisation der Sonnenkorona. *Astron. Nachrichten* **267**, 273. DOI ADS.
- Bemporad, A., Pagano, P.: 2015, Uncertainties in polarimetric 3D reconstructions of coronal mass ejections. *Astron. Astrophys.* **576**, A93. DOI ADS.
- Bird, M.K., Edenhofer, P.: 1990, Remote sensing observations of the solar corona. In: Schwenn, R., Marsch, E. (eds.) *Physics of the Inner Heliosphere I*, 13. DOI ADS.
- Bothmer, V., Schwenn, R.: 1998, The structure and origin of magnetic clouds in the solar wind. *Annales Geophysicae* **16**, 1. DOI ADS.
- Bunting, K.A., Barnard, L., Owens, M.J., Morgan, H.: 2024, Constraints on Solar Wind Density and Velocity Based on Coronal Tomography and Parker Solar Probe Measurements. *Astrophys. J.* **961**, 64. DOI ADS.
- Burlaga, L.F.: 1984, Magnetohydrodynamic Processes in the Outer Heliosphere. *Space Sci. Rev.* **39**, 255. DOI ADS.
- Cane, H.V., Richardson, I.G., St. Cyr, O.C.: 2000, Coronal mass ejections, interplanetary ejecta and geomagnetic storms. *Geophys. Res. Lett.* **27**, 3591. DOI ADS.
- Chifu, I.A.M.: 2015, Multi-spacecraft analysis of the solar coronal plasma. PhD thesis, Technical University of Braunschweig, Germany. ADS.
- Colaninno, R., Thernisien, A., Howard, R., Brechbiel, D., Dennison, H., Hess, P., Koss, S., Noya, M., Simon, W., Thompson, A., McMullin, D., Laut, S., Hunt, T., Gardner, L., Lanagan, A., Hagood, R., Hohl, B., Uhl, A., Smith, L., Zurcher, D., Stump, E., Newman, M., Ragan, T., Caron, J.: 2025, The Narrow Field Imager (NFI) for the Polarimeter to Unify the Corona and Heliosphere (PUNCH). *Sol. Phys.* **300**, 104. DOI ADS.
- Cranmer, S.R., van Ballegoijen, A.A., Edgar, R.J.: 2007, Self-consistent coronal heating and solar wind acceleration from anisotropic magnetohydrodynamic turbulence. *Astrophys. J. Suppl.* **171**, 520. DOI ADS.
- Cranmer, S.R., van Ballegoijen, A.A., Woolsey, L.N.: 2013, Connecting the Sun's high-resolution magnetic carpet to the turbulent heliosphere. *Astrophys. J.* **767**, 125. DOI ADS.
- Crifo, F., Picat, J.P., Cailloux, M.: 1983, Coronal Transients - Loop or Bubble. *Sol. Phys.* **83**, 143. DOI ADS.
- Dai, X., Wang, H., Inhester, B.: 2020, Electron Density Reconstruction of Solar Coronal Mass Ejections Based on a Genetic Algorithm: Method and Application. *Astrophys. J.* **896**, 155. DOI ADS.
- Dai, X., Wang, H., Huang, X., Du, Z., He, H.: 2014, The Classification of Ambiguity in Polarimetric Reconstruction of Coronal Mass Ejection. *Astrophys. J.* **780**, 141. DOI ADS.
- de Koning, C., Authors, O., Authors, O.O., Authors, O.O.O.: 2025, . *Solar Phys.*
- DeForest, C.E., de Koning, C.A., Elliott, H.A.: 2017a, 3D polarized imaging of coronal mass ejections: Chirality of a CME. *Astrophys. J.* **850**, 130. DOI ADS.
- DeForest, C.E., de Koning, C.A., Elliott, H.A.: 2017b, 3D Polarized Imaging of Coronal Mass Ejections: Chirality of a CME. *Astrophys. J.* **850**, 130. DOI ADS.
- DeForest, C.E., Howard, T.A., Tappin, S.J.: 2013a, The Thomson surface, II: Polarization. *Astrophys. J.* **765**, 44. DOI ADS.
- DeForest, C.E., Howard, T.A., Tappin, S.J.: 2013b, The Thomson Surface. II. Polarization. *Astrophys. J.* **765**. DOI.
- DeForest, C.E., Seaton, D.B., West, M.J.: 2022, Three-polarizer Treatment of Linear Polarization in Coronagraphs and Heliospheric Imagers. *Astrophys. J.* **927**, 98. DOI ADS.

-
- DeForest, C., Gibson, S., Killough, R., Waltham, N., Beasley, M., Colaninno, R., Laurent, G., Seaton, D., Hughes, M., Guhathakurta, M., Viall, N., Attie, R., Banerjee, D., Barnar, L., Biesecker, D., Bisi, M., Bothmer, V., Brody, A., Burkepille, J., Cairns, I., Campbell, J., david Cheney, Case, T., Caspi, A., Chhiber, R., Clapp, M., Cranmer, S., Davies, J., de Koning, C., Desai, M., Elliott, H., Farid, S., Gallardo-Lacourt, B., Gilly, C., Gobat, C., Hanson, M., Harrison, R., Hassler, D., Henley, C., Henry, A., Howard, R., Jackson, B., Jones, S., Kolinski, D., Lamb, D., Lehtinen, F., Lowder, C., Malanushenko, A., Matthaeus, W., McComas, D., McGee, J., Morgan, H., Oberoi, D., Odstrcil, D., Parmenter, C., Patel, R., Pecora, F., Persyn, S., Pizzo, V., Plunkett, S., Provornikova, E., Raouafi, N.E., Redfern, J., Rouillard, A., Smith, K., Smith, K., Talpas, Z., Tappin, J., Thernisien, A., Thompson, B., Kooten, S.V., Walsh, K., Webb, D., Wells, W., West, M., Wiens, Z., Yang, Y.: 2025, *Polarimeter to Unify the Corona and Heliosphere (PUNCH)*. Submitted to Solar Physics. <https://arxiv.org/abs/2509.15131>.
- Démoulin, P.: 2007, Quantitative links between CMEs and magnetic clouds. *Ann. Geophys.* **25**, 1.
- Dere, K.P., Wang, D., Howard, R.: 2005, Three-dimensional structure of coronal mass ejections from LASCO polarization measurements. *Astrophys. J. Lett.* **620**, L119. DOI. ADS.
- Edwards, L., Bunting, K.A., Ramsey, B., Gunn, M., Fearn, T., Knight, T., Muro, G.D., Morgan, H.: 2023, Derived electron densities from linear polarization observations of the visible-light corona during the 14 December 2020 total solar eclipse. *Solar Phys.* **298**, 140. DOI. ADS.
- Fan, Y.: 2018, MHD Simulation of a Prominence Eruption. *Astrophys. J.*
- Fisher, R., Guhathakurta, M.: 1995, Physical properties of polar coronal rays and holes as observed with the Spartan 201-01 coronagraph. *Astrophys. J. Lett.* **447**, L139. DOI. ADS.
- Floyd, O., Lamy, P.: 2019, Polarimetric reconstruction of coronal mass ejections from LASCO-C2 observations. *Solar Phys.* **294**, 168. DOI. ADS.
- Fränz, M., Harper, D.: 2002, Heliospheric coordinate systems. *planss* **50**, 217. DOI. ADS.
- Gibson, S.E., Fan, Y.: 2008, Partially-ejected flux ropes: implications for interplanetary coronal mass ejections. *J. Geophys. Res.* **113**. DOI.
- Gibson, S.E., Fludra, A., Bagenal, F., Biesecker, D., del Zanna, G., Bromage, B.: 1999, Solar minimum streamer densities and temperatures using Whole Sun Month coordinated data sets. *J. Geophys. Res.* **104**, 9691. DOI. ADS.
- Gibson, S.E., Fludra, A., Bagenal, F., Biesecker, D., Del Zanna, G., Bromage, B.: 1999, Solar minimum streamer densities and temperatures using Whole Sun Month coordinated data sets. *J. Geophys. Res.* **104**, 9691.
- Gibson, S., Kucera, T., White, S., Dove, J., Fan, Y., Forland, B., Rachmeler, L., Downs, C., Reeves, K.: 2016, FORWARD: A toolset for multiwavelength coronal magnetometry. *Front. Astron. Space Sci.* **3**.
- Gradshteyn, I.S., Ryzhik, I.M.: 2007, *Table of integrals, series, and products*, 7th edn. Elsevier/Academic Press, Amsterdam, xviii+1171. Translated from the Russian, Translation edited and with a preface by Alan Jeffrey and Daniel Zwillinger, With one CD-ROM (Windows, Macintosh and UNIX). ISBN 978-0-12-373637-6; 0-12-373637-4.
- Green, L.M., Kliem, B., Török, T., van Driel-Gesztelyi, L., Attrill, G.D.R.: 2007, Transient coronal sigmoids and rotating erupting flux ropes. *Solar Phys.* **246**, 345.
- Guhathakurta, M.: 1989, The Large and Small Scale Density Structure in the Solar Corona. PhD thesis, University of Denver, Colorado. ADS.
- Guhathakurta, M., Holzer, T.E., MacQueen, R.M.: 1996, The large-scale density structure of the solar corona and the heliospheric current sheet. *Astrophys. J.* **458**, 817. DOI. ADS.
- Guhathakurta, M., Fludra, A., Gibson, S.E., Biesecker, D., Fisher, R.: 1999, Physical properties of a coronal hole from a coronal diagnostic spectrometer, Mauna Loa Coronagraph, and LASCO observations during the Whole Sun Month. *J. Geophys. Res.* **104**, 9801.
- Gulisano, A.M., Démoulin, P., Dasso, S., Ruiz, M.E., Marsch, E.: 2010, Global and local expansion of magnetic clouds in the inner heliosphere. *Astron. Astrophys.* **509**, A39. DOI. ADS.
- Hildner, E., Gosling, J.T., Hansen, R.T., Bohlin, J.D.: 1975, The Sources of Material Comprising a Mass Ejection Coronal Transient. *Sol. Phys.* **45**, 363. DOI. ADS.
- Howard, T.A., DeForest, C.E.: 2012, The Thomson surface, I: Reality and myth. *Astrophys. J.* **752**, 130. DOI. ADS.
- Howard, T.A., Tappin, S.J.: 2009, Interplanetary Coronal Mass Ejections Observed in the Heliosphere: 1. Review of Theory. *Space Sci. Rev.* **147**, 31. DOI. ADS.

-
- Howard, T.A., Tappin, S.J., Odstrcil, D., DeForest, C.E.: 2013, The Thomson surface, III: Tracking features in 3D. *Astrophys. J.* **765**, 45. DOI ADS.
- Inhester, B.: 2015, Thomson scattering in the solar corona. *arXiv e-prints*, arXiv:1512.00651. DOI ADS.
- Jackson, B.V., Tokumaru, M., Iwai, K., Bracamontes, M.T., Buffington, A., Fujiki, K., Murakami, G., Heyner, D., Sanchez-Cano, B., Rojo, M., Aizawa, S., Andre, N., Barthe, A., Penou, E., Fedorov, A., Sauvaud, J.-A., Yokota, S., Saito, Y.: 2023, Forecasting Heliospheric CME Solar-Wind Parameters Using the UCSD Time-Dependent Tomography and ISEE Interplanetary Scintillation Data: The 10 March 2022 CME. *Sol. Phys.* **298**, 74. DOI ADS.
- Jarolim, R.e.a.: 2025,.
- Lamy, P.L., Gilardy, H., Llebaria, A.: 2022, Observations of the solar F-Corona from space. *Space Sci. Rev.* **218**, 53. DOI ADS.
- Lamy, P., Llebaria, A., Boclet, B., Gilardy, H., Burtin, M., Floyd, O.: 2020, Coronal Photopolarimetry with the LASCO-C2 Coronagraph over 24 Years [1996 - 2019]. *Sol. Phys.* **295**, 89. DOI ADS.
- Lamy, P., Gilardy, H., Llebaria, A., Quémerais, E., Hernandez, F.: 2021, LASCO-C3 observations of the K- and F-coronae over 24 Years (1996-2019): Photopolarimetry and electron density distribution. *Solar Phys.* **296**, 76. DOI ADS.
- Laurent, N.e.a.: 2025,.
- Leblanc, Y., Dulk, G.A., Bougeret, J.-L.: 1998, Tracing the electron density from the corona to 1 AU. *Solar Phys.* **183**, 165. DOI ADS.
- Linan, L., Baratashvili, T., Lani, A., Schmieder, B., Brchneleva, M., Guo, J.H., Poedts, S.: 2025, Coronal mass ejection propagation in the dynamically coupled space weather tool: COCONUT + EUHFORIA. *Astron. Astrophys.* **693**, A229. DOI ADS.
- Lionello, R., Downs, C., Mason, E.I., Linker, J.A., Caplan, R.M., Riley, P., Titov, V.S., DeRosa, M.L.: 2023, Global MHD Simulations of the Time-dependent Corona. *Astrophys. J.* **959**, 77. DOI ADS.
- López-Portela, C., Paz Miralles, M., Lara, A.: 2025, A Drag-force Analysis of Solar Wind White-light Tracers in the Inner Heliosphere. *Astrophys. J.* **990**, 116. DOI ADS.
- Lu, L., Inhester, B., Feng, L., Liu, S., Zhao, X.: 2017, Measure the Propagation of a Halo CME and Its Driven Shock with the Observations from a Single Perspective at Earth. *Astrophys. J.* **835**, 188. DOI ADS.
- Lugaz, N., Salman, T.M., Winslow, R.M., Al-Haddad, N., Farrugia, C.J., Zhuang, B., Galvin, A.B.: 2020, Inconsistencies Between Local and Global Measures of CME Radial Expansion as Revealed by Spacecraft Conjunctions. *Astrophys. J.* **899**, 119. DOI ADS.
- Malanushenko, A., Authors, O., Authors, O.O., Authors, O.O.O.: 2025, *Solar Phys.*.
- Mann, G., Warmuth, A., Vocks, C., Rouillard, A.P.: 2023, A heliospheric density and magnetic field model. *Astron. Astrophys.* **679**, A64. DOI ADS.
- Maruca, B.A., Qudsi, R.A., Alterman, B.L., Walsh, B.M., Korreck, K.E., Verscharen, D., Bandyopadhyay, R., Chhiber, R., Chasapis, A., Parashar, T.N., Matthaeus, W.H., Goldstein, M.L.: 2023, The trans-heliospheric survey: Radial trends in plasma parameters across the heliosphere. *Astron. Astrophys.* **675**, A196. DOI ADS.
- Mierla, M., Inhester, B., Marqué, C., Rodriguez, L., Gissot, S., Zhukov, A., Berghmans, D., Davila, J.: 2009, On 3D reconstruction of coronal mass ejections: I. Method description and application to SECCHI-COR data. *Solar Physics* **259**, 123.
- Mierla, M., Inhester, B., Antunes, A., Boursier, Y., Byrne, J.P., Colaninno, R., Davila, J., de Koning, C.A., Gallagher, P.T., Gissot, S., Howard, R.A., Howard, T.A., Kramar, M., Lamy, P., Liewer, P.C., Maloney, S., Marqué, C., McAteer, R.T.J., Moran, T., Rodriguez, L., Srivastava, N., Cyr, O.C.S., Stenborg, G., Temmer, M., Thernisien, A., Vourlidas, A., West, M.J., Wood, B.E., Zhukov, A.N.: 2010, On the 3-D reconstruction of Coronal Mass Ejections using coronagraph data. *Annales Geophysicae* **28**, 203. DOI <https://angeo.copernicus.org/articles/28/203/2010/>.
- Mierla, M., Chifu, I., Inhester, B., Rodriguez, L., Zhukov, A.: 2011, Low polarised emission from the core of coronal mass ejections. *Astron. Astrophys.* **530**, L1. DOI ADS.
- Mierla, M., Inhester, B., Zhukov, A.N., Shestov, S.V., Bemporad, A., Lamy, P., Koutchmy, S.: 2022, Polarimetric Studies of a Fast Coronal Mass Ejection. *Sol. Phys.* **297**, 78. DOI ADS.
- Minnaert, M.: 1930, On the continuous spectrum of the corona and its polarisation. *Z. Astrophys.* **1**, 209. ADS.

-
- Moraes Filho, V.P., Uritsky, V.M., Thompson, B.J., Gibson, S.E., DeForest, C.E.: 2024, SynCOM: An Empirical Model for High-resolution Simulations of Transient Solar Wind Flows. *Astrophys. J.* **975**, 294. DOI. ADS.
- Moran, T.G., Davila, J.M.: 2004, Three-dimensional polarimetric imaging of coronal mass ejections. *Science* **305**, 66. DOI. ADS.
- Moran, T.G., Davila, J.M., Thompson, W.T.: 2010, Three-dimensional polarimetric coronal mass ejection localization tested through triangulation. *Astrophys. J.* **712**, 453. DOI. ADS.
- Morgan, H., Cook, A.C.: 2020, The Width, Density, and Outflow of Solar Coronal Streamers. *Astrophys. J.* **893**, 57. DOI. ADS.
- Morgan, H., Byrne, J.P., Habbal, S.R.: 2012, Automatically Detecting and Tracking Coronal Mass Ejections. I. Separation of Dynamic and Quiescent Components in Coronagraph Images. *Astrophys. J.* **752**, 144. DOI. ADS.
- Munro, R.H., Jackson, B.V.: 1977, Physical properties of a polar coronal hole from 2 to 5 R_{\odot} . *Astrophys. J.* **213**, 874. DOI. ADS.
- Odstrcil, D.: 2023, Heliospheric 3-D MHD ENLIL simulations of multi-CME and multi-spacecraft events. *Frontiers in Astronomy and Space Sciences* **10**, 1226992. DOI. ADS.
- Öhman, Y.: 1947, Results from observations of the total solar eclipse of 1945 July 9: I. The polarization of the corona. *Stockholms Observatoriums Annaler* **15**, 2.1. ADS.
- Pagano, P., Bemporad, A., Mackay, D.H.: 2015, Future capabilities of CME polarimetric 3D reconstructions with the METIS instrument: A numerical test. *Astron. Astrophys.* **582**, A72. DOI. ADS.
- Pal, S.: 2022, Uncovering the process that transports magnetic helicity to coronal mass ejection flux ropes. *Advances in Space Research* **70**, 1601. DOI. ADS.
- Parker, E.N.: 1957, Sweet's Mechanism for Merging Magnetic Fields in Conducting Fluids. *JGR* **62**, 509. DOI. ADS.
- Pogorelov, N.V., Arge, C.N., Caplan, R.M., Colella, P., Linker, J.A., Singh, T., Van Straalen, B., Upton, L., Downs, C., Gebhart, C., Hegde, D.V., Henney, C., Jones, S., Johnston, C., Kim, T.K., Marble, A., Raza, S., Stulajter, M.M., Turtle, J.: 2024, Space Weather with Quantified Uncertainties: Improving Space Weather Predictions with Data-Driven Models of the Solar Atmosphere and Inner Heliosphere. In: *Journal of Physics Conference Series*, *Journal of Physics Conference Series* **2742**, 012013. DOI. ADS.
- Poland, A.I., Munro, R.H.: 1976, Interpretation of broad-band polarimetry of solar coronal transients: importance of the H α emission. *Astrophys. J.* **209**, 927. DOI. ADS.
- Provornikova, E., Merkin, V.G., Vourlidas, A., Malanushenko, A., Gibson, S.E., Winter, E., Arge, C.N.: 2024, MHD Modeling of a Geoeffective Interplanetary Coronal Mass Ejection with the Magnetic Topology Informed by In Situ Observations. *Astrophys. J.* **977**, 106. DOI. ADS.
- Provornikova, E., Authors, O., Authors, O.O., Authors, O.O.O.: 2025., *Solar Phys.*.
- Sachdeva, N., Tóth, G., Manchester, W.B., van der Holst, B., Huang, Z., Sokolov, I.V., Zhao, L., Shidi, Q.A., Chen, Y., Gombosi, T.I., Henney, C.J., Lloveras, D.G., Vázquez, A.M.: 2021, Simulating Solar Maximum Conditions Using the Alfvén Wave Solar Atmosphere Model (AWSOM). *Astrophys. J.* **923**, 176. DOI. ADS.
- Saito, K., Makita, M., Nishi, K., Hata, S.: 1970, A non-spherical axisymmetric model of the solar K corona of the minimum type. *Ann. Tokyo Astron. Obs.* **12**, 51. ADS.
- Schuster, A.: 1879, on the polarisation of the Solar Corona. *Mon. Not. R. Astron. Soc.* **40**, 35. DOI. ADS.
- Seaton, D., Authors, O., Authors, O.O., Authors, O.O.O., Authors, O.O.O.O.: 2025., *Solar Phys.*.
- Thernisien, A.F.R., Howard, R.A., Vourlidas, A.: 2006, Modeling of Flux Rope Coronal Mass Ejections. *Astrophys. J.* **652**, 763. DOI. ADS.
- Thernisien, A., Vourlidas, A., Howard, R.A.: 2009, Forward Modeling of Coronal Mass Ejections Using STEREO/SECCHI Data. *Solar Phys.* **256**, 111. DOI. ADS.
- van de Hulst, H.C.: 1950, The electron density of the solar corona. *Bull. Astron. Inst. Netherlands* **11**, 135. ADS.
- Vourlidas, A., Howard, R.A.: 2006, The proper treatment of coronal mass ejection brightness: A new methodology and implications for observations. *Astrophys. J.* **642**, 1216. DOI. ADS.
- Young, R.K.: 1911, *Polarization of the light in the solar corona*. ADS.
- Yurchyshyn, V., Wang, H., Abramenko, V.: 2003, How directions and helicity of erupted solar magnetic fields define geoeffectiveness of coronal mass ejections. *Advances in Space Research* **32**, 1965. DOI. ADS.

-
- Zhuang, B., Lugaz, N., Al-Haddad, N., Winslow, R.M., Scolini, C., Farrugia, C.J., Galvin, A.B.: 2023, Evolution of the Radial Size and Expansion of Coronal Mass Ejections Investigated by Combining Remote and In Situ Observations. *Astrophys. J.* **952**, 7. DOI. ADS.
- Zhuang, B., Lugaz, N., Wood, B.E., Braga, C.R., Temmer, M., Gou, T., Hess, P., Shaik, S.B., Cormack, C.M., Li, X.: 2025, Evolution of a Coronal Mass Ejection with an Eruptive Prominence from the Corona to Interplanetary Space. *Astrophys. J.* **990**, 181. DOI. ADS.
- Zhukov, A.N., Thizy, C., Galano, D., Bourgoignie, B., Dolla, L., Jean, C., Nicula, B., Shestov, S., Galy, C., Rougeot, R., Versluys, J., Zender, J., Lamy, P., Fineschi, S., Gunar, S., Inhester, B., Mierla, M., Rudawy, P., Tsinganos, K., Koutchmy, S., Howard, R., Peter, H., Vives, S., Abbo, L., Aime, C., Aleksiejuk, K., Baran, J., Bak-Steslicka, U., Bemporad, A., Berghmans, D., Besliu-Ionescu, D., Buckley, S., Buiu, O., Capobianco, G., Cimoch, I., DHuys, E., Dziezyc, M., Fleury-Frenette, K., Gibson, S.E., Giordano, S., Golub, L., Grochowski, K., Heinzl, P., Hermans, A., Jacobs, J., Jecic, S., Kranitis, N., Landini, F., Loreggia, D., Magdalenic, J., Maia, D., Marque, C., Melich, R., Morawski, M., Mosdorf, M., Noce, V., Orleanski, P., Paschalis, A., Peresty, R., Rodriguez, L., Seaton, D.B., Short, L., Simar, J.-F., Steslicki, M., Sorensen, R., Terrasa, G., Vooren, N.V., Verstringe, F., Zangrilli, L.: 2025, *The SPIICS solar coronagraph aboard the Proba-3 formation flying mission. Scientific objectives and instrument design.* <https://arxiv.org/abs/2509.00253>.